SIAM J. IMAGING SCIENCES
Vol. 9, No. 4, pp. 1525–1551

The Linearized Inverse Problem in Multifrequency Electrical Impedance Tomography*

Giovanni S. Alberti†, Habib Ammari†, Bangti Jin‡, Jin-Keun Seo§, and Wenlong Zhang¶

Abstract. This paper provides an analysis of the linearized inverse problem in multifrequency electrical impedance tomography. We consider an isotropic conductivity distribution with a finite number of unknown inclusions with different frequency dependence, as is often seen in biological tissues. We discuss reconstruction methods for both fully known and partially known spectral profiles and demonstrate in the latter case the successful employment of difference imaging. We also study the reconstruction with an imperfectly known boundary and show that the multifrequency approach can eliminate modeling errors and recover almost all inclusions. In addition, we develop an efficient group sparse recovery algorithm for the robust solution of related linear inverse problems. Several numerical simulations are presented to illustrate and validate the approach.

Key words. multifrequency electrical impedance tomography, linearized inverse problem, reconstruction, imperfectly known boundary, group sparsity, regularization

AMS subject classifications. 35R30, 49N45, 65N21, 92C55, 65F22

DOI. 10.1137/16M1061564

1. Introduction.

Electrical impedance tomography (EIT) is a diffusive imaging modality that allows recovering the conductivity of an electrically conducting object by using electrodes to measure the resulting voltage on its boundary, induced by multiple known injected currents. It is safe, cheap, and portable and is potentially applicable to clinical imaging in a range of areas. However, the EIT inverse problem is severely ill-posed and has thus shown only modest image quality when compared with other modalities [11]. This has motivated numerous mathematical studies on EIT imaging techniques including small anomaly conductivity imaging [7, 8, 10, 42] and hybrid conductivity imaging [2, 3, 4, 6, 9, 20, 56].

Static imaging aims at recovering absolute conductivity values. Apart from the popular linearization approach, a number of static imaging algorithms have been developed, e.g., the least-squares method [51, 14, 45, 34, 36], direct methods [57, 13, 44], and statistical methods

*Received by the editors February 16, 2016; accepted for publication (in revised form) July 6, 2016; published electronically October 4, 2016.
http://www.siam.org/journals/siims/9-4/M106156.html
Funding: This work was partially supported by the ERC Advanced Grant Project MULTIMOD-267184 and the EPSRC grant EP/M025160/1.
†Department of Mathematics, ETH Zürich, Rämistrasse 101, CH-8092 Zürich, Switzerland (giovanni.alberti@math.ethz.ch, habib.ammari@math.ethz.ch).
‡Department of Computer Science, University College London, Gower Street, London, WC1E 6BT, UK (bangti.jin@gmail.com, b.jin@ucl.ac.uk).
§Department of Computational Science and Engineering, Yonsei University, Seodaemun-Gu, Seoul 120-749, Korea (seoj@yonsei.ac.kr).
¶Department of Mathematics and Applications, École Normale Supérieure, 45 Rue d'Ulm, 75005 Paris, France (wenlong.zhang@ens.fr).

[37, 22]; see also the overviews [11, 46]. However, static imaging has so far achieved only limited success in practice, since electrode voltages are insensitive to localized conductivity changes but sensitive to forward modeling errors, e.g., boundary shape and electrode positions. Hence, apart from accurate data, a very accurate forward model is required for its success; however, this is often difficult to obtain in practice. A prominent idea is to use difference imaging, in the hope of canceling out modeling errors due to, e.g., boundary shape. A traditional approach is time difference imaging, which produces an image of the conductivity change by inverting a linearized sensitivity model. A second approach is multifrequency EIT (mfEIT), which has also attracted attention in recent years.

Imaging by mfEIT exploits the frequency dependence of the conductivity. Experimental research has found that the conductivity of many biological tissues varies strongly with the frequency [21, 19, 43]. In [5], the authors analytically exhibited fundamental mechanisms underlying the fact that effective electrical properties of biological tissue and their frequency dependence reflect the tissue composition and physiology, and a homogenization theory was developed. In mfEIT, boundary voltages are recorded simultaneously, while varying the modulation frequency of the injected current. It is expected to be especially useful for the diagnostic imaging of conditions such as acute stroke, brain injury, and breast cancer, because patients are admitted into care after the onset of the pathology and thus lack a baseline record for healthy tissue, so time difference imaging may not be used.

There have been several studies on frequency-difference imaging [26, 53, 63]. An mfEIT experimental design for head imaging was given in [63]. In these works, the simple frequency difference (between two neighboring frequencies) was often employed. Seo et al. [55] proposed a weighted frequency difference imaging technique, based on a suitable weighted voltage difference between any *two* sets of data. It was numerically shown that the approach can accommodate geometrical errors, including an imperfectly known boundary. This approach can improve the imaging quality when the background is frequency dependent. Recently, Malone et al. [47, 48] proposed a nonlinear reconstruction scheme, which uses all multifrequency data directly to recover the volume fractions of the tissues, and validated the approach on phantom experimental data. Harrach and Seo [27] developed a direct method for detecting inclusions from frequency-difference data. See also [39] for a recovery algorithm at low frequencies.

This work analyzes mfEIT in the linearized regime, by linearizing the forward model around a constant conductivity, as customarily adopted in practice. We shall discuss both the mathematically convenient continuum model and the practically popular complete electrode model. Our main contributions are as follows. First, we discuss mfEIT imaging for spectral profiles that are known, partially known, or unknown, and we also generalize existing studies, especially [55]. Second, we rigorously justify mfEIT for handling geometrical errors. Third, we present a novel group sparse reconstruction algorithm of iterative shrinkage type, which is easily implemented and converges quickly. Extensive numerical experiments confirm our discussions. All these findings provide new valuable insights into mfEIT, which are expected to be of great interest to the engineering community.

This paper is organized as follows. In section 2, we mathematically formulate mfEIT using a continuum model and analyze three important scenarios, depending on the knowledge of the spectral profiles. Then, in section 3, we illustrate the potential of mfEIT in handling the modeling errors due to an imperfectly known boundary shape. These analyses are then

extended to the complete electrode model in section 4. In section 5, we present a novel group sparse reconstruction algorithm. In section 6, extensive numerical experiments are presented to illustrate the approach. Finally, some concluding remarks are given in section 7.

2. The continuum model. In this section, we mathematically formulate mfEIT in the continuum model with a known boundary. Let $\Omega \subset \mathbb{R}^d$ $(d = 2, 3)$ be a bounded domain with a smooth boundary $\partial\Omega$. The forward problem reads as follows: for an input current $f \in L^2_\diamond(\partial\Omega) := \{g \in L^2(\partial\Omega) : \int_{\partial\Omega} g\, ds = 0\}$ and $\sigma(x,\omega)$, find $u(\cdot,\omega) \in H^1_\diamond(\Omega) := \{v \in H^1(\Omega) : \int_{\partial\Omega} v ds = 0\}$ such that:

$$\begin{cases} -\nabla \cdot (\sigma(x,\omega)\nabla u(x,\omega)) = 0 & \text{in } \Omega, \\ \sigma(x,\omega)\dfrac{\partial u}{\partial \nu} = f(x) & \text{on } \partial\Omega, \end{cases} \tag{2.1}$$

where ω is the frequency and ν is the unit outward normal vector to $\partial\Omega$. The weak formulation of problem (2.1) is to find $u = u(\cdot,\omega) \in H^1_\diamond(\Omega)$ such that

$$\int_\Omega \sigma \nabla u \cdot \nabla v\, dx = \int_{\partial\Omega} f v\, ds, \qquad v \in H^1(\Omega).$$

Throughout, we assume that the conductivity $\sigma(x,\omega)$ takes a separable form

$$\sigma(x,\omega) = \sum_{k=0}^{K} \sigma_k(x) s_k(\omega), \tag{2.2}$$

where $K+1$ is the number of spectral profiles, $\{s_k(\omega)\}_{k=0}^K$ are the (possibly only partially known) material spectra, also known as endmembers, and $\{\sigma_k(x)\}_{k=0}^K$ are scalar functions representing the corresponding proportions, also known as abundances in the hyperspectral unmixing literature [38]. Further, we shall assume

$$\begin{aligned} \sigma_0(x) &= 1 + \delta\sigma_0(x), \\ \sigma_k(x) &= \delta\sigma_k(x), \quad k = 1, \dots, K, \end{aligned}$$

where the $\delta\sigma_k$s, i.e., $\{\delta\sigma_k\}_{k=0}^K$, are small (in suitable $L^p(\Omega)$ norms) so that a linearized model is valid. The $\delta\sigma_k$s, including the background $\delta\sigma_0$, are all unknown, represent the small inclusions/anomalies in the object Ω, and have compact spatial supports that are disjoint from each other. We also assume that the background frequency $s_0(\omega)$ is known.

Now we apply N linearly independent input currents $\{f_n\}_{n=1}^N \subset L^2_\diamond(\partial\Omega)$. Let $\{u_n \equiv u_n(\cdot,\omega)\}_{n=1}^N \subset H^1_\diamond(\Omega)$ be the corresponding solutions to (2.1), i.e.,

$$\int_\Omega \sigma \nabla u_n \cdot \nabla v\, dx = \int_{\partial\Omega} f_n v\, ds, \qquad v \in H^1(\Omega). \tag{2.3}$$

The inverse problem is to recover $\delta\sigma_k$s from $\{u_n(x,\omega)\}_{n=1}^N$ on $\partial\Omega$ at the frequencies $\{\omega_q\}_{q=1}^Q$.

Next we derive the linearized model for the inverse problem, based on an integral representation. Let $v_m \in H^1_\diamond(\Omega)$ be the potential corresponding to the unperturbed conductivity $\sigma_0(x,\omega) \equiv s_0(\omega)$ with the input current $f_m \in L^2_\diamond(\partial\Omega)$, namely,

$$\int_\Omega \sigma_0 \nabla v_m \cdot \nabla v\, dx = \int_{\partial\Omega} f_m v\, ds, \qquad v \in H^1(\Omega). \tag{2.4}$$

Then $v_m = v_m^*/s_0(\omega)$, where v_m^* is the solution of (2.4) corresponding to the case $s_0 \equiv 1$. Namely, the dependence of v_m on the frequency ω is explicit. Using (2.3) and (2.4), we obtain

$$\sum_{k=0}^{K} s_k(\omega) \int_\Omega \delta\sigma_k \nabla u_n \cdot \nabla v_m \, dx = \int_{\partial\Omega} (f_n v_m - f_m u_n) \, ds.$$

Hence, using the approximation $\nabla u_n(x,\omega) \approx \nabla v_n(x,\omega)$ in Ω (valid in the linear regime) and the identity $v_m = v_m^*/s_0(\omega)$, we arrive at a linearized model:

$$\sum_{k=0}^{K} s_k(\omega) \int_\Omega \delta\sigma_k \nabla v_n^* \cdot \nabla v_m^* \, dx = s_0(\omega)^2 \int_{\partial\Omega} (f_n v_m - f_m u_n) \, ds. \tag{2.5}$$

The right-hand side of (2.5) can be treated as a known quantity: u_n is the measured voltage data (and thus depends on ω), and v_m is computable. Next, we triangulate Ω into a shape-regular quasi-uniform mesh $\{\Omega_l\}_{l=1}^L$ and consider a piecewise constant approximation of $\delta\sigma_k$:

$$\delta\sigma_k(x) \approx \sum_{l=1}^{L} (\delta\sigma_k)_l \chi_{\Omega_l}(x), \quad k = 0, 1, \ldots, K, \tag{2.6}$$

where χ_{Ω_l} is the characteristic function of the lth element Ω_l, and $(\delta\sigma_k)_l$ denotes the corresponding value of $\delta\sigma_k$. Thus we get a finite-dimensional linear inverse problem

$$\sum_{k=0}^{K} s_k(\omega) \sum_{l=1}^{L} (\delta\sigma_k)_l \int_{\Omega_l} \nabla v_n^* \cdot \nabla v_m^* \, dx = s_0(\omega)^2 \int_{\partial\Omega} (f_n v_m - f_m u_n) \, ds.$$

Throughout, we shall focus on the *finite-dimensional* linear inverse problem, where the discretization is always assumed to be adequate. We refer interested readers to [49] for discussions on the interplay between regularization, discretization, and noise level.

Last, we introduce the sensitivity matrix M and the data vector X. We use a single index $j = 1, \ldots, J$ with $J = N^2$ for the index pair (m,n) with $j = N(m-1)+n$ and introduce the frequency-independent sensitivity matrix $M = [M_{jl}] \in \mathbb{R}^{J \times L}$ with its entries M_{jl} given by

$$M_{jl} = \int_{\Omega_l} \nabla v_n^* \cdot \nabla v_m^* \, dx \quad (j \leftrightarrow (m,n)).$$

Likewise, we introduce a vector $X(\omega) \in \mathbb{R}^J$ with its jth entry $X_j(\omega)$ given by

$$X_j(\omega) = s_0(\omega)^2 \int_{\partial\Omega} (f_n v_m(\omega) - f_m u_n(\omega)) \, ds \quad (j \leftrightarrow (m,n)).$$

By writing $A_k = (\delta\sigma_k)_l \in \mathbb{R}^L$, $k = 0, \ldots, K$, we obtain a linear system (parameterized by ω)

$$M \sum_{k=0}^{K} s_k(\omega) A_k = X(\omega). \tag{2.7}$$

Remark 1. In (2.7), the sensitivity matrix M is identical with that in static imaging, and hence mfEIT does not lead to improved resolution. Namely, in mfEIT the diffusive nature of the modality does not change with the frequency ω. But as we shall see below, in the presence of spectral contrast, mfEIT does allow recovering $\{A_k\}_{k=0}^K$ and removing modeling errors.

In mfEIT, A_ks are of primary interest. Depending on the a priori spectral knowledge, we discuss the following three cases separately: (a) all s_ks are known; (b) s_ks may not be fully known, but with substantially different frequency dependence; (c) s_ks are only partially known, and we aim at a partial recovery of A_ks. They are of different degrees of challenge.

2.1. Case (a): Known spectral profiles. First we consider the case when s_ks are all known. In some applications, this is feasible, since the spectral profiles of many materials can be measured (see, e.g., [18] for tissues). Suppose that we can measure $X(\omega)$ at Q distinct frequencies $\{\omega_q\}_{q=1}^Q$. By writing $S = (S_{kq}) \in \mathbb{R}^{(K+1)\times Q}$ with $S_{kq} = s_k(\omega_q)$, we get from (2.7)

$$MAS = X, \tag{2.8}$$

where the matrix $X = [X(\omega_1) \ \dots \ X(\omega_Q)] \in \mathbb{R}^{J\times Q}$. In (2.8), the matrix M can be precomputed, and the matrix S and the data X are known: only $A = [A_0 \ \dots \ A_K] \in \mathbb{R}^{L\times(K+1)}$ is unknown. It is natural to assume that a sufficient number of frequencies are taken so that S is incoherent, namely, $Q \geq K+1$ and $\operatorname{rank}(S) = K+1$ (and presumably S is also well-conditioned). Then S admits a right inverse S^{-1}. By letting $Y = XS^{-1}$ we obtain

$$MA = Y.$$

These are $K+1$ decoupled linear system. By letting $Y = [Y_0 \ \dots \ Y_K] \in \mathbb{R}^{J\times(K+1)}$, we have

$$MA_k = Y_k, \quad k = 0, \dots, K, \tag{2.9}$$

where A_k represents the kth abundance. Here each linear system determines one and only one abundance A_k. The stable and accurate solution of (2.9) will be discussed in section 5.

The condition $\operatorname{rank}(S) = K+1$ is necessary and sufficient for a full decoupling, and the well-conditioning of S ensures a stable decoupling. It specifies the condition under which the abundance unmixing is practically feasible and also the proper selection of $\{\omega_q\}_{q=1}^Q$ such that $\operatorname{rank}(S) = K+1$. It depends essentially on the incoherence of $\{s_k(\omega)\}_{k=0}^K$, without which a full decoupling is impossible. For example, consider the simple case of two endmembers with $s_0(\omega) = 1+\omega$, $s_1(\omega) = 2+2\omega$. Then for any $Q > 1$, S is always of rank one.

The right inverse $Y = XS^{-1}$ can also be viewed as a least-squares procedure

$$\min_{Y\in\mathbb{R}^{J\times(K+1)}} \|X - YS\|_F.$$

Thus, for a rank-deficient S, our approach yields the minimum-norm matrix Y compatible with the data, and for an inconsistent S, it yields a best approximation via projection. By the perturbation theory for least-squares problems [25], the well-conditioning of S implies that the procedure is stable with respect to small perturbations in the spectral profiles.

This approach generalizes the weighted frequency difference EIT (fdEIT) method [55].

Example 1. Consider the case with $K = 1$ and $Q = 2$, i.e., two frequencies. We write

$$X = [X(\omega_1)\ X(\omega_2)] \quad \text{and} \quad S = \begin{bmatrix} s_0(\omega_1) & s_0(\omega_2) \\ s_1(\omega_1) & s_1(\omega_2) \end{bmatrix}.$$

Therefore, if S is invertible, we obtain

$$Y = XS^{-1} = \frac{s_0(\omega_1)}{\det S}\left[\frac{s_1(\omega_2)}{s_0(\omega_1)}X(\omega_1) - \frac{s_1(\omega_1)}{s_0(\omega_1)}X(\omega_2) \quad X(\omega_2) - \frac{s_0(\omega_2)}{s_0(\omega_1)}X(\omega_1)\right].$$

The second column of Y recovers the weighted fdEIT method [55]. Thus our method generalizes [55]. Our approach directly incorporates multifrequency data, which improves the numerical stability, especially in the presence of strong correlation between neighboring frequencies and imprecisely known spectral profiles. Further, it enables decoupling multiple inclusions. In the special case $s_0(\omega_1) = s_0(\omega_2)$, it recovers the usual frequency difference. This delineates the region of validity of frequency difference for multifrequency data.

Remark 2. The minimal number Q of frequencies is equal to $K + 1$, provided that with $\{\omega_q\}_{q=1}^{Q}$, S is sufficiently incoherent, i.e., $\operatorname{rank}(S) = K+1$. With an inadvertently poor choice of $\{\omega_q\}_{q=1}^{Q}$, it may require more than $K + 1$ frequencies to achieve the desired incoherence.

2.2. Case (b): Spectral profiles with substantially different frequency dependence. Next we consider the case when some of (or, possibly, all) $s_k(\omega)$s are not known but do not change rapidly with ω, when compared to the remaining ones. Thus, instead of using $X(\omega)$ directly, it is natural to differentiate (2.7) with respect to ω to eliminate the contributions from those $s_k(\omega)$s that do not vary much with ω. This discriminating effect is useful in practice. For example, the conductivity of malign tissues is more sensitive with respect to frequency variations in a certain frequency range [59, 43], even though that of healthy tissues in the background may exhibit fairly complex structure.

More precisely, let $\mathcal{P} \subseteq \{0, 1, \ldots, K\}$ be such that

$$|s_p'(\omega_q)| \gg |s_k'(\omega_q)|, \qquad p \in \mathcal{P}, k \in \{0, 1, \ldots, K\} \setminus \mathcal{P}. \tag{2.10}$$

By differentiating (2.7) with respect to ω and invoking the assumption (2.10), we obtain

$$M \sum_{p\in\mathcal{P}} A_p s_p'(\omega) \approx X'(\omega). \tag{2.11}$$

Thus the contributions from the remaining profiles are negligible. Different reconstruction schemes should be used depending on whether the spectral profiles $\{s_p(\omega)\}_{p\in\mathcal{P}}$ are known.

2.2.1. Case (b1): The spectral profiles $\{s_p(\omega)\}_{p\in\mathcal{P}}$ are not known. In the case when the spectral profiles $\{s_p(\omega)\}_{p\in\mathcal{P}}$ are not known, (2.11) cannot be simplified further. By solving (2.11), we can recover at most $\sum_{p\in\mathcal{P}} s_p'(\omega)A_p$, namely, a linear combination of the inclusions. Since the weights $\{s_p'(\omega)\}_{p\in\mathcal{P}}$ are unknown, it is impossible to separate $\{A_p, p \in \mathcal{P}\}$. However, when $\mathcal{P} = \{p\}$ (i.e., $|\mathcal{P}| = 1$), $\delta\sigma_p$ may be recovered up to a multiplicative constant, which gives the support information. We illustrate the technique with an example.

Example 2. Consider the case $K = 1$ and two linear frequency profiles, i.e., $s_0(\omega) = \alpha_0 + \beta_0\omega$ and $s_1(\omega) = \alpha_1 + \beta_1\omega$ with $\beta_0 \ll \beta_1$. Then the differentiation imaging amounts to

$$\beta_0 MA_0 + \beta_1 MA_1 = X'(\omega).$$

If MA_0 and MA_1 are comparable, then $\beta_0 \ll \beta_1$ implies that the contribution of $\beta_0 MA_0$ to the data is negligible. Hence, the technique allows one to recover the component $\beta_1 MA_1$, which upon linear inversion yields $\beta_1 A_1$. In particular, it gives the support $\mathrm{supp}(A_1)$ and also its magnitude up to a multiplicative constant. Further, for known β_1, it allows recovering A_1.

2.2.2. Case (b2): The spectral profiles $\{s_p(\omega)\}_{p\in\mathcal{P}}$ are known. If the spectral profiles $\{s_p(\omega)\}_{p\in\mathcal{P}}$ are known, it is possible to perform the same analysis of Case (a) to (2.11). Taking measurements at Q distinct frequencies $\omega_1, \dots, \omega_Q$, we have

$$M \sum_{p\in\mathcal{P}} A_p s_p'(\omega_q) \approx X'(\omega_q), \qquad q = 1, \dots, Q.$$

Then, with $\widetilde{S} = (\widetilde{S}_{pq}) \in \mathbb{R}^{|\mathcal{P}|\times Q}$, $\widetilde{S}_{pq} = s_p'(\omega_q)$, $X' = [X'(\omega_1) \ \dots \ X'(\omega_Q)] \in \mathbb{R}^{J\times Q}$, we get $MA\widetilde{S} = X'$. Then the inversion step is completely analogous to that in section 2.1, if $\operatorname{rank}\widetilde{S} = |\mathcal{P}|$ (and well-conditioning). All the inclusions A_p, $p \in \mathcal{P}$, can be recovered.

2.2.3. Numerical implementation. In the implementation, we take

$$M \sum_{k=0}^{K} A_k \frac{s_k(\omega_{q+1}) - s_k(\omega_q)}{\omega_{q+1} - \omega_q} = \frac{X(\omega_{q+1}) - X(\omega_q)}{\omega_{q+1} - \omega_q}. \tag{2.12}$$

It approximates the derivative $s_k'(\omega_q)$ with the forward difference $s_k'(\omega_q) \approx (s_k(\omega_{q+1}) - s_k(\omega_q))/(\omega_{q+1} - \omega_q)$. One can also use higher-order difference formulas, and they represent different ways to perform difference imaging. Their robustness with respect to noise might differ due to the ill-posed nature of numerical differentiation. In this work, we shall use (2.12).

2.3. Case (c): Partially known spectral profiles, partial recovery of the abundances. In practice, it is also of interest to recover some information about $\{A_k\}$ when $\{s_k(\omega)\}$ are only partially known. Generally, this is infeasible. But, one can still obtain some information under certain a priori knowledge. To this end, recall the notation $Y_k = MA_k$; cf. (2.9). Then

$$Y_0 s_0(\omega_q) + \cdots + Y_K s_K(\omega_q) = X(\omega_q), \qquad q = 1, \dots, Q. \tag{2.13}$$

Now suppose the frequency dependence of $\{s_k(\omega)\}_{k=0}^K$ is of polynomial type, namely, $s_k(\omega) = \sum_{n=0}^N \alpha_k^n \omega^n$. Inserting this expression into (2.13) yields $\sum_{n=0}^N \sum_{k=0}^K (\alpha_k^n Y_k)\omega^n = X(\omega)$. By taking a sufficiently large number of modulating frequencies $\{\omega_q\}_{q=1}^Q$ (to be more precise, $Q \geq N+1$), and using the identity principle for polynomials, we can compute $B_n := \sum_{k=0}^K \alpha_k^n Y_k$, $n = 0, \dots, N$. Note that adding more frequencies does not tell more about Y_k and α_k^j than $\{B_n\}_{n=0}^N$. Namely, $\{B_n\}_{n=0}^N$ contain the essential information in $\{X(\omega_q)\}_{q=1}^Q$. Depending on K, N, and further a prior knowledge, some Y_k can be recovered without knowing the corresponding spectral profiles. Instead of providing a general analysis of all possible cases, we present two examples that explain the different situations that may appear.

Example 3. Consider the case $K = 1$. For every n we have $B_0 = \alpha_0^0 Y_0 + \alpha_1^0 Y_1$ and $B_n = \alpha_0^n Y_0 + \alpha_1^n Y_1$, whence $Y_1 = (\alpha_0^0\alpha_1^n - \alpha_1^0\alpha_0^n)^{-1}(\alpha_0^0 B_n - \alpha_0^n B_0)$. Since s_0 is known, so are α_0^0 and α_0^n. Hence, Y_1 may be recovered up to a multiplicative constant c, if $\alpha_0^0\alpha_1^n - \alpha_1^0\alpha_0^n \neq 0$, without assuming any knowledge of $s_1(\omega)$. This condition simply represents the incoherence between s_0 and s_1. Finally, by solving $MA_1 = cY_1$, $\delta\sigma_1$ can be recovered up to some constant.

Further, assuming a unique recovery of the linearized inverse problem, the knowledge of B_0 allows recovering an unknown linear combination of A_0 and A_1, especially the union of their supports. Since the supports of A_0 and A_1 are assumed to be disjoint from each other, this allows recovering $\mathrm{supp}(A_0)$, given that $\mathrm{supp}(A_1)$ has already been recovered.

Example 4. Note that if $K = 2$ and $N = 1$, we get only

$$\alpha_0^0 Y_0 + \alpha_1^0 Y_1 + \alpha_2^0 Y_2 = B_0 \quad \text{and} \quad \alpha_0^1 Y_0 + \alpha_1^1 Y_1 + \alpha_2^1 Y_2 = B_1,$$

which is vastly insufficient to determine all the unknowns. However, a calculation similar to Example 3 shows that the support of Y_2 can be determined if $K = N = 2$ and s_1 is known, if a certain incoherence condition is satisfied. Like before, by solving the underdetermined system $MA_2 = cY_2$, we can recover the support of $\delta\sigma_2$. Further, assuming a unique recovery with the linearized inverse problem, $\mathrm{supp}(\delta\sigma_0)$ and $\mathrm{supp}(\delta\sigma_1)$ may be determined.

With obvious modifications, the preceding discussion is also valid for more general basis functions $\phi_n(\omega)$ which form a unisolvent system on the set $\{\omega_q\}_{q=1}^Q$ [17, pp. 31–32].

3. Imperfectly known boundary. Now we illustrate the potentials of mfEIT for handling modeling errors, e.g., an imperfectly known boundary, which has long been one of the main obstacles in practice [1, 40, 41]. The use of a slightly incorrect boundary can lead to large reconstruction errors, and mfEIT is one strategy to overcome the challenge [55]. Here we present an analysis of the approach in the linearized regime to justify these numerical findings.

We denote the true but unknown physical domain by $\widetilde{\Omega}$ and the computational domain by Ω. Next we introduce a forward map $F : \widetilde{\Omega} \to \Omega$, $\widetilde{x} \mapsto x$, which is assumed to be a smooth orientation preserving map with a smooth inverse map $F^{-1} : \Omega \to \widetilde{\Omega}$. We denote the Jacobian of the map F by J_F and the Jacobian of F with respect to the surface integral by J_F^S.

Now suppose that the function $\widetilde{u}_n(\widetilde{x},\omega) \in H^1_\diamond(\widetilde{\Omega})$ satisfies (2.1) in the true domain $\widetilde{\Omega}$ with a conductivity $\widetilde{\sigma}(\widetilde{x},\omega)$ and input current $\widetilde{f}_n \in L^2_\diamond(\partial\widetilde{\Omega})$, namely,

$$\begin{cases} -\nabla_{\widetilde{x}} \cdot (\widetilde{\sigma}(\widetilde{x},\omega)\nabla_{\widetilde{x}}\widetilde{u}_n(\widetilde{x},\omega)) = 0 & \text{in } \widetilde{\Omega}, \\ \widetilde{\sigma}(\widetilde{x},\omega)\dfrac{\partial\widetilde{u}_n(\widetilde{x},\omega)}{\partial\widetilde{\nu}} = \widetilde{f}_n & \text{on } \partial\widetilde{\Omega}. \end{cases} \tag{3.1}$$

Here the conductivity $\widetilde{\sigma}(\widetilde{x},\omega)$ takes a separable form (cf. (2.2))

$$\widetilde{\sigma}(\widetilde{x},\omega) = \sum_{k=0}^{K} s_k(\omega)\widetilde{\sigma}_k(\widetilde{x}) \tag{3.2}$$

with $\widetilde{\sigma}_0(\widetilde{x}) = 1 + \delta\widetilde{\sigma}_0(\widetilde{x})$, and $\widetilde{\sigma}_k(\widetilde{x}) = \delta\widetilde{\sigma}_k(\widetilde{x})$, $k = 1, \ldots, K$, where $\delta\widetilde{\sigma}_k$s are small and their supports are disjoint and stay away from $\partial\widetilde{\Omega}$. The weak formulation (by suppressing the

dependence on ω) is given by the following: find $\widetilde{u}_n(\cdot,\omega) \in H^1_\diamond(\widetilde{\Omega})$ such that

$$\int_{\widetilde{\Omega}} \widetilde{\sigma}\nabla_{\widetilde{x}}\widetilde{u}_n \cdot \nabla_{\widetilde{x}}\widetilde{v}d\widetilde{x} = \int_{\partial\widetilde{\Omega}} \widetilde{f}_n\widetilde{v}d\widetilde{s}, \qquad \widetilde{v} \in H^1(\widetilde{\Omega}). \tag{3.3}$$

Let us now discuss the experimental setup. The practitioner chooses a current density $f_n \in L^2_\diamond(\partial\Omega)$ defined on $\partial\Omega$. It is then applied to the unknown boundary $\partial\widetilde{\Omega}$. The applied current $\widetilde{f}_n$ on $\partial\widetilde{\Omega}$ results to be

$$\widetilde{f}_n = (f_n \circ F)|\det J_F^S|. \tag{3.4}$$

This implies $\int_{\partial\widetilde{\Omega}} \widetilde{f}_n d\widetilde{s} = 0$, whence problem (3.1) is well-posed. This induces the potential $\widetilde{u}_n \in H^1_\diamond(\widetilde{\Omega})$ given by (3.3), which should be measured on $\partial\widetilde{\Omega}$. However, due to the incorrect knowledge of the boundary, the measured quantity is in fact $u_n := \widetilde{u}_n \circ F^{-1}$ restricted to $\partial\Omega$.

Remark 3. The current density on $\partial\widetilde{\Omega}$ is locally defined by $\widetilde{J} = I/\mathrm{area}(\widetilde{A})$, where I is the current injected through a small surface $\widetilde{A} \subseteq \partial\widetilde{\Omega}$. Thus $\widetilde{J} = \frac{I}{\mathrm{area}(\widetilde{A})} = \frac{I}{\mathrm{area}(A)}\frac{\mathrm{area}(A)}{\mathrm{area}(\widetilde{A})} = J\frac{\mathrm{area}(A)}{\mathrm{area}(\widetilde{A})}$, where J is the current density on $A := F(\widetilde{A}) \subseteq \partial\Omega$. Hence, $|\det J_F^S|$ is the infinitesimal version of $\frac{\mathrm{area}(A)}{\mathrm{area}(\widetilde{A})}$. Since $\int_{\partial\widetilde{\Omega}} \widetilde{f}_n\widetilde{u}_n d\widetilde{s} = \int_{\partial\Omega} f_n u_n\, ds$ and $\int_{\partial\Omega} f_n u_n\, ds$ denotes the power needed to maintain the potential u_n on $\partial\Omega$, the choice (3.4) preserves the needed power for the data.

We consider only the case that Ω is a small variation of $\widetilde{\Omega}$ (but comparable with $\delta\sigma_k$) so that the linearized regime is valid. We write $F : \widetilde{\Omega} \to \Omega$ by $F(\widetilde{x}) = \widetilde{x} + \epsilon\widetilde{\phi}(\widetilde{x})$, where $\epsilon > 0$ is small and the smooth function $\widetilde{\phi}(\widetilde{x})$ characterizes the deformation. Let $F^{-1}(x) = x + \epsilon\phi(x)$ be the inverse, which is also smooth. To examine its influence on the linearized inverse problem, we introduce $v_m \in H^1_\diamond(\Omega)$ corresponding to $\sigma_0(x,\omega) = s_0(\omega)$ in Ω and the flux f_m, i.e.,

$$\int_\Omega \sigma_0\nabla v_m \cdot \nabla v\, dx = \int_{\partial\Omega} f_m v\, ds, \qquad v \in H^1(\Omega). \tag{3.5}$$

We can now state the corresponding linearized inverse problem. The proof shows that even for an isotropic $\widetilde{\sigma}$ in $\widetilde{\Omega}$, cf. (3.2), in Ω the equivalent σ is generally anisotropic.

Proposition 1. *Set $\delta\sigma_k = \delta\widetilde{\sigma}_k \circ F^{-1}$ for $k = 0, 1, \ldots, K$ and $v_m^* = s_0(\omega)v_m$ for $m = 1, \ldots, N$. The linearized inverse problem on the computational domain Ω is given by*

$$s_0(\omega)\epsilon\int_\Omega \Psi\nabla v_n^* \cdot \nabla v_m^*\, dx + \sum_{k=0}^{K} s_k(\omega)\int_\Omega \delta\sigma_k\nabla v_n^* \cdot \nabla v_m^*\, dx = s_0(\omega)^2\int_{\partial\Omega}(f_n v_m - f_m u_n)\, ds \tag{3.6}$$

for some smooth function $\Psi : \Omega \to \mathbb{R}^{d\times d}$, which is independent of the frequency ω.

Proof. First, we derive the governing equation for the variable $u_n = \widetilde{u}_n \circ F^{-1}$ in the domain Ω from (3.3). Denote by $v = \widetilde{v} \circ F^{-1} \in H^1(\Omega)$. By the chain rule we have $\nabla_{\widetilde{x}}\widetilde{u}_n \circ F^{-1} = (J_F^t \circ F^{-1})\nabla_x u_n$, where the superscript t denotes the matrix transpose. Thus, we deduce

$$\int_{\widetilde{\Omega}} \widetilde{\sigma}\nabla_{\widetilde{x}}\widetilde{u}_n \cdot \nabla_{\widetilde{x}}\widetilde{v}d\widetilde{x} = \int_\Omega \sigma\nabla u_n \cdot \nabla v\, dx,$$

where the transformed conductivity $\sigma(x,\omega)$ is given by [60, 40, 41]

$$\sigma(x,\omega) = \left(\frac{J_F(\cdot)\widetilde{\sigma}(\cdot,\omega)J_F^t(\cdot)}{|\det J_F(\cdot)|} \circ F^{-1} \right)(x). \tag{3.7}$$

Moreover, by (3.4) we have $\int_{\partial\widetilde{\Omega}} \widetilde{f}_n \widetilde{v} d\widetilde{s} = \int_{\partial\Omega} f_n v \, ds$. Hence, by (3.3) the potential u_n satisfies

$$\int_\Omega \sigma \nabla u_n \cdot \nabla v \, dx = \int_{\partial\Omega} f_n v \, ds, \qquad v \in H^1(\Omega). \tag{3.8}$$

Then by choosing $v = v_m$ in (3.8) and $v = u_n$ in (3.5), we arrive at

$$\int_\Omega (\sigma - \sigma_0)\nabla u_n \cdot \nabla v_m \, dx = \int_{\partial\Omega} (f_n v_m - f_m u_n) \, ds. \tag{3.9}$$

Note that $J_F = I + \epsilon J_{\widetilde{\phi}}$, and $J_{F^{-1}} = I + \epsilon J_\phi = I - \epsilon J_{\widetilde{\phi}} \circ F^{-1} + O(\epsilon^2)$, since ϵ is small. Since $|\det J_F| = 1 + \epsilon \mathrm{div}\widetilde{\phi} + O(\epsilon^2)$ [28, equation (2.10)], $\sigma(x,\omega)$ can be written as

$$\begin{aligned}
\sigma(x,\omega) &= \widetilde{\sigma}(\cdot,\omega)(1+\epsilon \mathrm{div}\widetilde{\phi}(\cdot))^{-1}(I + \epsilon(J_{\widetilde{\phi}}(\cdot) + J_{\widetilde{\phi}}^t(\cdot))) \circ F^{-1}(x) + O(\epsilon^2) \\
&= \widetilde{\sigma}(\cdot,\omega)((1-\epsilon \mathrm{div}\widetilde{\phi}(\cdot))I + \epsilon(J_{\widetilde{\phi}}(\cdot) + J_{\widetilde{\phi}}^t(\cdot))) \circ F^{-1}(x) + O(\epsilon^2) \\
&= \widetilde{\sigma}(\cdot,\omega) \circ F^{-1}(x) + \Psi(x)\epsilon + O(\epsilon^2),
\end{aligned}$$

where $\Psi = (J_{\widetilde{\phi}} + J_{\widetilde{\phi}}^t - \mathrm{div}\widetilde{\phi} I) \circ F^{-1}$ is independent of ω. Thus we obtain,

$$\sigma(x,\omega) \approx s_0(\omega) I + \epsilon s_0(\omega)\Psi(x) + \sum_{k=0}^{K} \delta\sigma_k(x) s_k(\omega) I. \tag{3.10}$$

Substituting it into (3.9) and invoking the approximation $\nabla u_n \approx \nabla v_n$ completes the proof. ∎

By Proposition 1, in the presence of an imperfectly known boundary with the deformation magnitude ϵ comparable with $\{\delta\sigma_k\}_{k=0}^K$, there is a dominant source of errors in (3.6): it contains an additional anisotropic component $\epsilon\Psi$. Thus a direct inversion of (3.6) is unsuitable. This explains the observation that a slightly incorrect boundary can lead to erroneous recoveries [1, 24]. This issue can be resolved by mfEIT. Indeed, by rearranging (3.6) we obtain

$$s_0(\omega)\int_\Omega (\epsilon\Psi + \delta\sigma_0)\nabla v_n^* \cdot \nabla v_m^* \, dx + \sum_{k=1}^{K} s_k(\omega) \int_\Omega \delta\sigma_k \nabla v_n^* \cdot \nabla v_m^* \, dx = s_0(\omega)^2 \int_{\partial\Omega} (f_n v_m - f_m u_n) \, ds. \tag{3.11}$$

This is analogous to (2.5), with the only difference lying in the extra term $\epsilon\Psi$. Hence, all methods in section 2 are applicable. The inclusion $\delta\sigma_0$ will never be properly recovered, due to the pollution of the term $\epsilon\Psi$. However, $\{\delta\sigma_k(\omega)\}_{k=1}^K$ may be reasonably recovered, since they are affected slightly by the deformation only through $\delta\sigma_k = \delta\widetilde{\sigma}_k \circ F^{-1}$. Thus, mfEIT can effectively eliminate modeling errors caused by the boundary uncertainty.

4. The complete electrode model. In this section we adapt the approach discussed in sections 2 and 3 to the more realistic complete electrode model (CEM).

4.1. Perfectly known boundary. First we consider the case of a perfectly known boundary. Let Ω be an open bounded domain in $\mathbb{R}^d$ $(d = 2, 3)$ with a smooth boundary $\partial\Omega$. We denote the set of electrodes by $\{e_j\}_{j=1}^E \subset \partial\Omega$, which are disjoint from each other, i.e., $\bar{e}_i \cap \bar{e}_k = \emptyset$ if $i \neq k$. The applied current on the jth electrode e_j is denoted by I_j, and the current vector $I = (I_1, \ldots, I_E)^t$ satisfies $\sum_{j=1}^E I_j = 0$ by the law of charge conservation. Let the space $\mathbb{R}^E_\diamond$ be the subspace of $\mathbb{R}^E$ with zero mean, i.e., $I \in \mathbb{R}^E_\diamond$. The electrode voltages $U = (U_1, \ldots, U_E)^t$ are also grounded so that $U \in \mathbb{R}^E_\diamond$. Then the CEM reads as follows [12, 58]: given the conductivity $\sigma(x, \omega)$, positive contact impedances $\{z_j\}_{j=1}^E$, and an input current $I \in \mathbb{R}^E_\diamond$, find the potential $u(\cdot, \omega) \in H^1(\Omega)$ and the electrode voltages $U \in \mathbb{R}^E_\diamond$ such that

$$
\begin{cases}
-\nabla \cdot (\sigma(x,\omega)\nabla u(x,\omega)) = 0 \text{ in } \Omega, \\
u + z_j \dfrac{\partial u}{\partial \nu_\sigma} = U_j \text{ on } e_j,\ j = 1, 2, \ldots, E, \\
\displaystyle\int_{e_j} \frac{\partial u}{\partial \nu_\sigma}\, ds = I_j \text{ for } j = 1, 2, \ldots, E, \\
\dfrac{\partial u}{\partial \nu_\sigma} = 0 \text{ on } \partial\Omega \backslash \cup_{j=1}^E e_j,
\end{cases}
\tag{4.1}
$$

where $\frac{\partial u}{\partial \nu_\sigma}$ denotes the co-normal derivative $(\sigma\nabla u) \cdot \nu$. The second line describes the contact impedance effect. In practice, the contact impedances $\{z_j\}_{j=1}^E$ are observed to be inversely proportional to the conductivity of the object [30, 32], i.e.,

$$
z_j = s_0(\omega)^{-1} c_j \tag{4.2}
$$

for some constants $c_j > 0$ independently of ω, since by assumption, near $\partial\Omega$ we have $\sigma(x, \omega) = s_0(\omega)$. The weak formulation is given by the following: find $(u, U) \in \mathbb{H} := H^1(\Omega) \times \mathbb{R}^E_\diamond$ such that [23]

$$
\int_\Omega \sigma \nabla u \cdot \nabla v\, dx + \sum_{j=1}^E z_j^{-1} \int_{e_j} (u - U_j)(v - V_j)\, ds = \sum_{j=1}^E I_j V_j, \qquad (v, V) \in \mathbb{H}.
$$

The bilinear form defined on the left-hand side is coercive and continuous on $\mathbb{H}$, and thus by the Lax–Milgram theorem there exists a unique solution $(u(\cdot, \omega), U(\omega)) \in \mathbb{H}$.

Consider N input currents $\{I_n\}_{n=1}^N \subset \mathbb{R}^E_\diamond$, and let $\{(u_n, U_n)\}_{n=1}^N \subset \mathbb{H}$ be the corresponding solutions to (4.1), i.e., for all $(v, V) \in \mathbb{H}$

$$
\int_\Omega \sigma \nabla u_n \cdot \nabla v\, dx + \sum_{j=1}^E z_j^{-1} \int_{e_j} (u_n - U_{n,j})(v - V_j)\, ds = \sum_{j=1}^E I_{n,j} V_j. \tag{4.3}
$$

The electrode voltages $U_n \in \mathbb{R}^E_\diamond$ can be measured and are used to recover the conductivity $\sigma(x, \omega)$. To derive a linearized model, let $(v_m, V_m) \in \mathbb{H}$ be the solution corresponding to the reference conductivity $\sigma_0(x, \omega) = s_0(\omega)$: for every $(v, V) \in \mathbb{H}$ we have

$$
\int_\Omega \sigma_0 \nabla v_m \cdot \nabla v\, dx + \sum_{j=1}^E z_j^{-1} \int_{e_j} (v_m - V_{m,j})(v - V_j)\, ds = \sum_{j=1}^E I_{m,j} V_j. \tag{4.4}
$$

By (4.2), we can write $(v_m^*, V_m^*) = s_0(\omega)(v_m, V_m)$ for the solution (v_m^*, V_m^*) corresponding to $\sigma_0 \equiv 1$. Now we assume that $\sigma(x,\omega)$ follows (2.2). Using (4.3) and (4.4), we deduce

$$\sum_{k=0}^{K} s_k(\omega) \int_\Omega \delta\sigma_k \nabla u_n \cdot \nabla v_m \, dx = \sum_{j=1}^{E} (I_{n,j} V_{m,j} - I_{m,j} U_{n,j}).$$

Then, under the approximation $\nabla u_n \approx \nabla v_n$ in the domain Ω, and the approximation (2.6) of the inclusions $\delta\sigma_k$s on the triangulation $\{\Omega_l\}_{l=1}^L$, we have

$$\sum_{k=0}^{K} s_k(\omega) \sum_{l=1}^{L} (\delta\sigma_k)_l \int_{\Omega_l} \nabla v_n^* \cdot \nabla v_m^* \, dx = s_0(\omega)^2 \sum_{j=1}^{E} (I_{n,j} V_{m,j} - I_{m,j} U_{n,j}). \tag{4.5}$$

This formula is almost identical with (2.5), and formally their only difference lies in the computation of $X(\omega)$. Hence, all the discussions in section 2 can be adapted to the CEM (4.1). In particular, all inversion methods therein can be directly applied to this case.

4.2. Imperfectly known boundary. Now we consider the case of an imperfectly known boundary. Like before, let $\widetilde{\Omega}$ be the unknown true domain with a smooth boundary $\partial\widetilde{\Omega}$, and Ω be the computational domain with a smooth boundary $\partial\Omega$. Accordingly, let $\{\widetilde{e}_j\}_{j=1}^E \subset \partial\widetilde{\Omega}$ and $\{e_j\}_{j=1}^E \subset \partial\Omega$ be the real and computational electrodes, respectively, and assume they satisfy the usual conditions discussed above. Then we introduce a smooth orientation preserving forward map $F : \widetilde{\Omega} \to \Omega$ with a smooth inverse $F^{-1} : \Omega \to \widetilde{\Omega}$, and we denote the restriction of F to the boundary $\partial\widetilde{\Omega}$ by $f : \partial\widetilde{\Omega} \to \partial\Omega$. We write $F^{-1}(x) = x + \epsilon\phi(x)$, where $\epsilon > 0$ denotes the deformation magnitude. Further, it is assumed that there is no further electrode movement, i.e., $e_j = f(\widetilde{e}_j)$, $j = 1, \ldots, E$. With the conductivity $\widetilde{\sigma}(\widetilde{x},\omega)$ of the form (3.2) and input current $I_n \in \mathbb{R}^E_\diamond$, by (4.1), the quantity $(\widetilde{u}_n(\widetilde{x},\omega), \widetilde{U}_n(\omega)) \in \widetilde{\mathbb{H}} \equiv H^1(\widetilde{\Omega}) \times \mathbb{R}^E_\diamond$ satisfies

$$\begin{cases} -\nabla_{\widetilde{x}} \cdot (\widetilde{\sigma}(\widetilde{x},\omega) \nabla_{\widetilde{x}} \widetilde{u}_n(\widetilde{x},\omega)) = 0 \quad \text{in } \widetilde{\Omega}, \\ \displaystyle\int_{\widetilde{e}_j} \frac{\partial \widetilde{u}_n}{\partial \widetilde{\nu}_{\widetilde{\sigma}}} d\widetilde{s} = I_{n,j} \quad \text{on } \widetilde{e}_j, j = 1, 2, \ldots, E, \\ \displaystyle z_j \frac{\partial \widetilde{u}_n}{\partial \widetilde{\nu}_{\widetilde{\sigma}}} + \widetilde{u}_n = \widetilde{U}_{n,j} \quad \text{on } \widetilde{e}_j, j = 1, 2, \ldots, E, \\ \displaystyle \frac{\partial \widetilde{u}_n}{\partial \widetilde{\nu}_{\widetilde{\sigma}}} = 0 \quad \text{on } \partial\widetilde{\Omega} \setminus \cup_{j=1}^E \widetilde{e}_j. \end{cases} \tag{4.6}$$

The weak formulation is given by the following: find $(\widetilde{u}_n, \widetilde{U}_n) \in \widetilde{\mathbb{H}}$ such that for every $(\widetilde{v}, \widetilde{V}) \in \widetilde{\mathbb{H}}$

$$\int_{\widetilde{\Omega}} \widetilde{\sigma} \nabla_{\widetilde{x}} \widetilde{u}_n \cdot \nabla_{\widetilde{x}} \widetilde{v} \, d\widetilde{x} + \sum_{j=1}^{E} z_j^{-1} \int_{\widetilde{e}_j} (\widetilde{u}_n - \widetilde{U}_{n,j})(\widetilde{v} - \widetilde{V}_j) \, d\widetilde{s} = \sum_{j=1}^{E} I_{n,j} \widetilde{V}_j.$$

In the experimental setting, on Ω, the injected current $I_n \in \mathbb{R}^E_\diamond$ on the electrodes $\{e_j\}_{j=1}^E$ is known, and the corresponding voltage $\widetilde{U}_n(\omega) \in \mathbb{R}^E_\diamond$ can be measured. The inverse problem is to recover $\{\delta\widetilde{\sigma}_k\}_{k=0}^K$ from the voltages $\{\widetilde{U}_n(\omega)\}_{n=1}^N \subset \mathbb{R}^E_\diamond$ at $\{\omega_q\}_{q=1}^Q$.

Now we can state the corresponding linearized inverse problem for (4.6). Consider the potential $u_n(\cdot,\omega) = \widetilde{u}_n(\cdot,\omega)\circ F^{-1}$ and the associated electrode voltages $U_n = \widetilde{U}_n$.

Proposition 2. *Let the reference solutions $(v_m, V_m) \in \mathbb{H}$ be defined by (4.4) and the conductivity $\widetilde{\sigma}$ be of the form (3.2). Set $z = |\det J^S_{F^{-1}}|$, $\delta\sigma_k = \delta\widetilde{\sigma}_k \circ F^{-1}$ for $k = 0, 1, \dots, K$ and $(v_m^*, V_m^*) = s_0(\omega)(v_m, V_m)$ for $m = 1, \dots, N$. The linearized inverse problem on Ω is given by*

$$s_0(\omega)\epsilon \int_\Omega \Psi\nabla v_n^*\cdot\nabla v_m^*\,dx + \sum_{k=0}^{K} s_k(\omega)\int_\Omega \delta\sigma_k\nabla v_n^*\cdot\nabla v_m^*\,dx = s_0(\omega)^2\sum_{j=1}^{E}(I_{n,j}V_{m,j} - I_{m,j}U_{n,j}) - s_0(\omega)\sum_{j=1}^{E} c_j\int_{e_j}(z-1)\left(\frac{\partial v_m^*}{\partial\nu}\right)^2 ds \tag{4.7}$$

for some smooth function $\Psi : \Omega \to \mathbb{R}^{d\times d}$, which is independent of the frequency ω.

Proof. Proceeding as in the proof of Proposition 1, by a change of variables (and suppressing the variable ω), since $e_j = f(\widetilde{e}_j)$ we deduce

$$\int_{\widetilde{\Omega}} \widetilde{\sigma}\nabla_{\widetilde{x}}\widetilde{u}_n\cdot\nabla_{\widetilde{x}}\widetilde{v}d\widetilde{x} = \int_\Omega (\widetilde{\sigma}\circ F^{-1})(J_F^t\circ F^{-1})\nabla u_n\cdot(J_F^t\circ F^{-1})\nabla v|\det J_{F^{-1}}|dx$$

and

$$\int_{\widetilde{e}_j}(\widetilde{u}_n - \widetilde{U}_{n,j})(\widetilde{v} - \widetilde{V}_j)d\widetilde{s} = \int_{e_j}(u_n - U_{n,j})(v - V_j)|\det J^S_{F^{-1}}|\,ds,$$

where $v = \widetilde{v}\circ F^{-1} \in H^1(\Omega)$ and $V_j = \widetilde{V}_j$. Hence, $(u_n(\cdot,\omega), U_n(\omega))$ satisfies for every $(v, V) \in \mathbb{H}$

$$\int_\Omega \sigma\nabla u_n\cdot\nabla v\,dx + \sum_{j=1}^{E} z_j^{-1}\int_{e_j}(u_n - U_{n,j})(v - V_j)z\,ds = \sum_{j=1}^{E} I_{n,j}V_j,$$

where $\sigma(x,\omega)$ is given by (3.7). By combining this identity with (4.4), we obtain

$$\int_\Omega(\sigma-\sigma_0)\nabla u_n\cdot\nabla v_m\,dx = \sum_{j=1}^{E}(I_{n,j}V_{m,j} - I_{m,j}U_{n,j}) + \sum_{j=1}^{E}\int_{e_j}(z-1)(u_n - U_{n,j})\frac{\partial v_m}{\partial\nu_{\sigma_0}}\,ds.$$

In view of [28, 29], $z = 1 + \epsilon(\mathrm{Div}\phi_t - (d-1)H\phi_\nu) + O(\epsilon^2)$, where Div denotes the surface divergence, ϕ_t and ϕ_ν denote the tangential and normal components of the vectorial function ϕ on $\partial\Omega$, respectively, and H is the mean curvature of $\partial\Omega$. In particular, $z - 1 = O(\epsilon)$. Thus, by linearization we have

$$\int_{e_j}(z-1)(u_n - U_{n,j})\frac{\partial v_m}{\partial\nu_{\sigma_0}}\,ds \approx \int_{e_j}(z-1)(v_n - V_{n,j})\frac{\partial v_m}{\partial\nu_{\sigma_0}}\,ds = -z_j\int_{e_j}(z-1)\left(\frac{\partial v_m}{\partial\nu_{\sigma_0}}\right)^2 ds.$$

Inserting this approximation in the above identity we obtain

$$\int_\Omega(\sigma-\sigma_0)\nabla u_n\cdot\nabla v_m\,dx = \sum_{j=1}^{E}(I_{n,j}V_{m,j} - I_{m,j}U_{n,j}) - \sum_{j=1}^{E} z_j\int_{e_j}(z-1)\left(\frac{\partial v_m}{\partial\nu_{\sigma_0}}\right)^2 ds.$$

Using (4.2), the rest of the proof follows as in Proposition 1, and thus it is omitted. ∎

By proceeding as in the continuum model, we can rewrite (4.7) as

$$s_0(\omega)\int_\Omega(\epsilon\Psi+\delta\sigma_0)\nabla v_n^*\cdot\nabla v_m^*\,dx+\sum_{k=1}^K s_k(\omega)\int_\Omega\delta\sigma_k\nabla v_n^*\cdot\nabla v_m^*\,dx \tag{4.8}$$
$$=s_0(\omega)^2\sum_{j=1}^E(I_{n,j}V_{m,j}-I_{m,j}U_{n,j})-s_0(\omega)\sum_{j=1}^E c_j\int_{e_j}(z-1)\left(\frac{\partial v_m^*}{\partial\nu}\right)^2 ds.$$

When compared with (3.11), we observe the presence of the additional error term $s_0(\omega)C_m$, where $C_m := -\sum_{j=1}^E c_j\int_{e_j}(z-1)(\frac{\partial v_m^*}{\partial\nu})^2\,ds$, which comes from the boundary deformation. The formula (4.8) is consistent with (3.11): in the continuum case, the contact impedance effect is not present, and $u_n = U_n$ on the electrodes, namely, $c_j = 0$, whence $C_m = 0$.

All the preceding analysis easily carries over to the case $c_j > 0$. Before treating the general case, let us consider the simple scenario where $z \equiv 1$ on the electrodes $\cup_j e_j$.

Example 5. Recall that $z(x) = |\det J_{F^{-1}}^S(x)|$ for $x \in \partial\Omega$. Physically, the factor z represents the length/area deformation relative to the map $F^{-1}\colon \partial\Omega \to \partial\widetilde{\Omega}$. Thus, it may be reasonable to assume that the parametrization of the electrodes $\{e_j\}_{j=1}^E$ is known, which implies $z \equiv 1$ on the electrodes $\cup_j e_j$. Then we have $C_m \equiv 0$, whence

$$s_0(\omega)\int_\Omega(\epsilon\Psi+\delta\sigma_0)\nabla v_n^*\cdot\nabla v_m^*\,dx+\sum_{k=1}^K s_k(\omega)\int_\Omega\delta\sigma_k\nabla v_n^*\cdot\nabla v_m^*\,dx=s_0(\omega)^2\sum_{j=1}^E(I_{n,j}V_{m,j}-I_{m,j}U_{n,j}).$$

This identity is similar to (3.11), and the comments on the recovery issue remain valid, since the right-hand side is known. Thus, by applying any of the techniques in section 2, it is possible to eliminate the error $\epsilon\Psi$ due to the domain deformation, as this affects only the inclusion $\delta\sigma_0$. All the other inclusions $\{\delta\sigma_k\}_{k=1}^K$ may be successfully recovered.

Now we consider the general case $z \not\equiv 1$ on $\cup_j e_j$, i.e., the length (or the area) of the electrodes is not precisely known. However, since the error term C_m is independent of ω, the difference imaging in section 2.2 may be applied, provided that $0 \notin \mathcal{P}$, i.e., if the frequency profile $s_0(\omega)$ does not vary much with respect to ω. Then $s_0(\omega)C_m$ disappears upon differentiating (4.8), and the inversion step may be performed as in section 2.2.

The method of section 2.1 may also be applied, since the error term $s_0(\omega)C_m$ depends only on $s_0(\omega)$. Namely, its influence on the inversion step is lumped into $\delta\sigma_0$, like the conductivity perturbation $\epsilon\Psi$. Thus, all the inclusions $\{\delta\sigma_k\}_{k=1}^K$ may be recovered. Alternatively, one may see this as follows. When multiplying the system of equations associated to (4.8) by S^{-1}, the error term $s_0(\omega)C_m$ cancels out in all the systems $MA_k = Y_k$, for $k = 1, \dots, K$:

$$[s_0(\omega_1)C\,,\,\dots\,,\,s_0(\omega_Q)C]\,S^{-1} = C\,[s_0(\omega_1)\,,\,\dots\,,\,s_0(\omega_Q)]\begin{bmatrix} s_0(\omega_1) & \cdots & s_0(\omega_Q)\\ \vdots & \vdots & \vdots\\ s_K(\omega_1) & \cdots & s_K(\omega_Q)\end{bmatrix}^{-1}$$
$$= [C\,,\,0\,,\,\dots\,,\,0],$$

where C denotes the column vector corresponding to C_m.

5. Group sparse reconstruction algorithm. For all the scenarios discussed in the previous sections, one arrives at a number of (decoupled) linear systems

$$MA_k = Y_k, \quad k = 0, \dots, K, \tag{5.1}$$

where $M \in \mathbb{R}^{J\times L}$, $A_k \in \mathbb{R}^L$, and $Y_k \in \mathbb{R}^J$. The linear systems are often underdetermined, and severely ill-conditioned, due to the ill-posed nature of the EIT inverse problem. Below we describe a heuristic and yet very effective strategy for the stable and accurate solution of (5.1); we refer to [52, 54, 33] for general discussions on regularization methods.

There are several natural aspects for the regularization term, especially sparsity, grouping, disjoint sparsity, and bound constraints.

(1) For every k, the abundance $A_k = (\delta\sigma_k)_l \in \mathbb{R}^L$ is sparse with respect to the pixel basis. This suggests minimizing

$$\min_{A_k\in\Lambda} \|A_k\|_1 \quad \text{subject to } \|MA_k - Y_k\| \le \epsilon_k$$

for each $k = 0, \dots, K$. Here $\|\cdot\|_1$ denotes the ℓ^1 norm of a vector. The set Λ represents a box constraint on A_k, since σ is bounded from below and above by positive constants, due to physical constraint, and $\epsilon_k > 0$ is the estimated noise level of Y_k.

(2) In EIT applications, each A_k is often clustered, and this refers to the concept of group sparsity. The grouping can remove undesirable spikes often observed in the recoveries using the ℓ^1 penalty alone. This can be achieved by, e.g., elastic net [35]. In this work, we shall exploit the dynamic group sparsity (DGS) [31], which dynamically realizes group sparsity without knowing the supports of the A_ks.

(3) The supp(A_k)s are disjoint from each other. The disjoint supports of A_ks can be promoted, e.g., by penalizing the scalar product of the absolute values of the A_ks [62].

Next we develop an algorithm, termed as group iterative soft thresholding (GIST), for achieving the above goals. It combines the strengths of iterative soft thresholding (IST) [16] and DGS [31]: IST is easy to implement and has a built-in regularizing effect, whereas DGS encourages the group sparsity pattern. It is a simple modification of the IST (by omitting the subscript k): given an initial guess A^0, construct an approximation iteratively by

$$A^{j+1} = S_{s^j\alpha}(g^j),$$

where the proxy g^j is defined by

$$g^j = A^j - s^j M^t(MA^j - Y). \tag{5.2}$$

Note that $M^t(MA^j - Y)$ is the gradient of $\frac{1}{2}\|MA - Y\|^2$ at A^j. The scalar $\alpha > 0$ is a regularization parameter, and $s^j > 0$ is the step length. One simple choice of s^j is the constant one $s^j = 1/\|M\|^2$, which ensures the convergence of IST [16]. The operator S_λ for $\lambda > 0$ is defined by $S_\lambda(t) = \max(|t| - \lambda, 0)\,\mathrm{sign}(t)$ and applied componentwise for a vectorial argument.

In GIST, instead of performing the thresholding on g^j directly, we take into account the neighboring influence. This can be achieved by computing a generalized proxy d_l^j by [31]

$$d_l^j = |g_l^j|^2 + \sum_{k\in\mathcal{N}_l} w_{lk}|g_k^j|^2, \qquad l = 1, \dots, L, \tag{5.3}$$

where $w_{lk} \geq 0$ are weights, and $\mathcal{N}_l$ denotes the neighborhood of the lth element. The weights w_{lk} determine the correlation strength: the smaller w_{lk} is, the weaker the correlation between the lth and kth components is, and if $w_{lk} = 0$ for all $k \in \mathcal{N}_l$, it does not promote grouping at all. In our implementation, we take $w_{lk} = \beta$ for some $\beta > 0$ for all $k \in \mathcal{N}_l$, with a default value $\beta = 0.5$, and $\mathcal{N}_l$ consists of all elements in the triangulation that share one edge with the lth element. Then d^j is used to reweigh the thresholding step by

$$\bar{d}^j = \max(d^j)^{-1} d^j. \tag{5.4}$$

It indicates a normalized grouping effect: the larger $\bar{d}_l^j$ is, the more likely the lth element belongs to the group, and thus less thresholding should be applied. This can be achieved by rescaling α to be proportional to $(\bar{d}_l^j)^{-1}$ with a spatially variable regularization parameter

$$\bar{\alpha}_l^j = \alpha / \bar{d}_l^j, \quad l = 1, \ldots, L, \tag{5.5}$$

and last perform the projected thresholding with $\bar{\alpha}^j$

$$A^{j+1} = P_\Lambda(S_{s^j \bar{\alpha}^j}(g^j)), \tag{5.6}$$

where P_Λ denotes the pointwise projection onto the set Λ. The complete procedure is listed in Algorithm 1. Here $N \in \mathbb{N}$ is the maximum number of iterations, and the initial guess A^0 is the zero vector. The parameter α plays a crucial role in the performance of the algorithm: the larger α is, the sparser the recovered A is. There are several strategies available for its choice, e.g., the discrepancy principle and balancing principle [33]. One can terminate the algorithm by monitoring the relative change of the iterates.

Algorithm 1. Group iterative soft thresholding.

1: Input M, Y, W, $\mathcal{N}$, α, N and A^0.
2: **for** $j = 1, \ldots, N$ **do**
3: Compute the proxy g^j by (5.2).
4: Compute the generalized proxy d^j by (5.3).
5: Compute the normalized proxy $\bar{d}^j$ by (5.4).
6: Adapt the regularization parameter $\bar{\alpha}^j$ by (5.5).
7: Update the abundance A^{j+1} by the group thresholding (5.6).
8: Check the stopping criterion.
9: **end for**

Last, disjoint sparsity can also be enforced in Algorithm 1. Specifically, we first compute $\bar{d}^{k,j}$ for A_k separately according to (5.4) and then at each $l = 1, \ldots, L$, update them by

$$\bar{d}_l^{k,j} = \begin{cases} \bar{d}_l^{k,j} & \text{if } k = k_l^*, \\ \varepsilon & \text{otherwise,} \end{cases} \qquad k_l^* = \underset{k=0,\ldots,K}{\arg\max}\ \bar{d}_l^{k,j},$$

where $\varepsilon > 0$ is a small number to avoid numerical overflow. It only retains the most likely abundance (with the likelihood for A_k given by $\bar{d}^{k,j}$) and hence enforces the disjoint sparsity.

Remark 4. The theoretical analysis of the dynamic group sparse recovery is still unavailable, except for compressed sensing problems [31]. However, it does not cover the EIT inverse problem, due to a lack of the restricted isometry property.

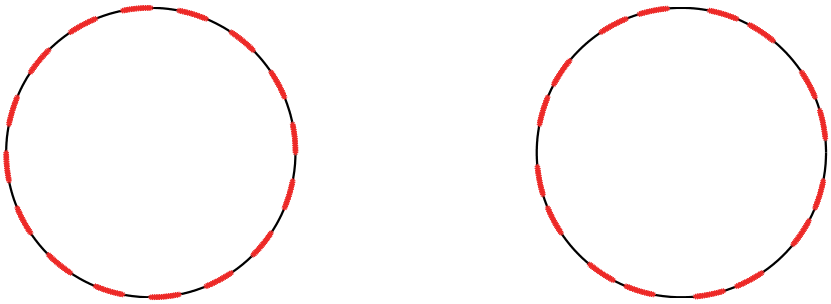

(a) computational domain Ω (b) imperfectly known electrode positions

Figure 1. *Electrode arrangement for the computational domain Ω and for imperfectly known electrode positions (used in Example 10). The curved segments in red denote the electrodes.*

6. Numerical experiments and discussions. Now we present numerical results to illustrate the analytic study. We consider only the CEM (4.1), since the results for (2.1) are similar. The experimental setup is as follows. The computational domain Ω is taken to be the unit circle $\Omega = \{(x_1, x_2) : x_1^2 + x_2^2 < 1\}$. There are sixteen electrodes $\{e_j\}_{j=1}^E$ (with $E = 16$) evenly placed along the boundary $\partial\Omega$, each of length $\pi/16$, thus occupying one half of $\partial\Omega$; cf. Figure 1(a). Unless otherwise specified, the contact impedances $\{z_j\}_{j=1}^E$ on the electrodes $\{e_j\}_{j=1}^E$ are all set to unit, and $\sigma_0 \equiv 1$. Further, we assume that $s_0(\omega)$ for the background is $s_0(\omega) \equiv 1$. This is not a restriction, since $s_0(\omega)$ is known, and one can rescale $s_k(\omega)$s so that $s_0 \equiv 1$. We measure U for all 15 sinusoidal input currents. The model (4.1) is discretized using a piecewise linear FEM on a shape regular quasi-uniform triangulation of Ω [23]. For the inversion, the conductivity is represented on a coarser mesh using a piecewise constant basis. Then the noisy data U^δ is generated by adding Gaussian noise to the exact data $U^\dagger := U(\sigma^\dagger)$ corresponding to the true conductivity $\sigma^\dagger(x, \omega)$ as follows:

$$U_j^\delta = U_j^\dagger + \epsilon \max_l |U_l^\dagger - U_l(\sigma_0)|\varepsilon_j, \quad j = 1, \ldots, E,$$

where ϵ is the relative noise level, and ε_j follows the standard normal distribution.

Remark 5. Colton and Kress [15, pp. 121, 289] coined the term *inverse crime* to denote the act of employing the *same* model to generate and to invert synthetic data. Inverse crime often leads to excellent reconstructions without revealing the ill-posed nature of inverse problems and hence has to be avoided in numerical experiments. In section 6.1, we have employed a finer mesh to generate the data than for inversion, in order to alleviate the inverse crime; and in section 6.2, the meshes for generating the data and inversion are completely different.

We shall present numerical results for the cases of a perfectly known and of an imperfectly known boundary separately and discuss only cases (a) and (b) with spectral profiles that are either fully known or have substantially different frequency dependence. Case (c) will not be discussed since the inversion is analogous to case (a). To solve (5.1), we use Algorithm 1 with a constant step size. The scalar α was determined in a trial-and-error manner, and set to 10^{-2} for all examples below, unless otherwise specified. We did not implement disjoint sparsity,

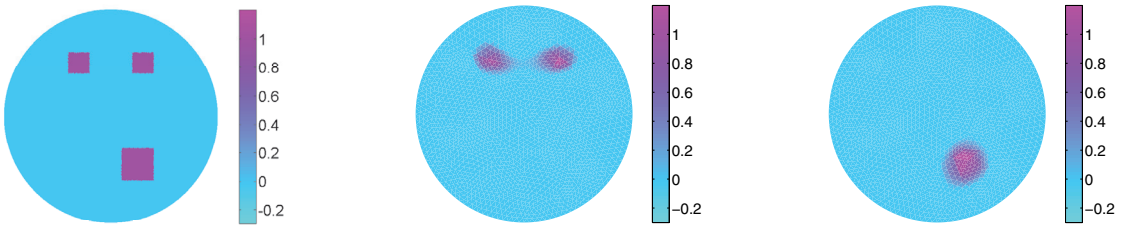

(a) true $\delta\sigma_k$s (b) recovered $\delta\sigma_1$ (c) recovered $\delta\sigma_2$

Figure 2. *Numerical results for Example* 6(i) *with* 1% *data noise and fully known* $s_k(\omega)$*s. The recoveries are obtained using the direct approach.*

since in all examples below the recoveries are already very satisfactory. The algorithm is always initialized with a zero vector. Numerically, it converges steadily and fast, and for the examples presented below, it takes about 8 seconds per recovery. All the computations were performed using MATLAB 2013a on a 2.5G Hz and 6G RAM personal laptop.

6.1. Perfectly known boundary. First, we consider the case of a known boundary.

Example 6. Consider three square inclusions: the two inclusions on the top share the same spectral profile $s_1(\omega)$, and the one on the bottom has a second spectral profile $s_2(\omega)$; cf. Figure 2(a) for an illustration. In the experiments, we consider the following two cases:

(i) The spectral profiles are $s_1(\omega) = 0.1\omega + 0.1.$ and $s_2(\omega) = 0.2\omega$.
(ii) The spectral profiles are $s_1(\omega) = 0.1\omega + 0.1$ and $s_2(\omega) = 0.02\omega$.

In either case, we take $Q = 3$ frequencies, $\omega_1 = 0$, $\omega_2 = 0.5$ and $\omega_3 = 1$.

The results for Example 6 with $\epsilon = 1\%$ data noise are shown in Figures 2 and 6 for cases 6(i) and 6.1(ii), respectively. In case 6(i), the two frequencies have about the same magnitude, and the matrix S is nonsingular. The direct approach in section 2.1 separates the two sets of inclusions well thanks to the spectral incoherence. The recovery is very localized within a clean background, the supports match closely the true ones (and are clearly disjoint from each other), and their magnitudes are well retrieved. The latter observation is a distinct feature of the proposed GIST in section 5. Hence, for known incoherent profiles, the inclusions can be fairly recovered. It is noteworthy that our approach is insensitive to model parameters: see Figure 3 for the recoveries with different contact impedance constants. Case 6(ii) is similar, except that the variation of $s_2(\omega)$ is much smaller. The preceding observations remain largely valid, except that the inclusion $\delta\sigma_2$ has minor spurious oscillations. This is attributed to the presence of data noise: the noise is comparable with inclusion contributions. Hence, for the accurate recovery, the data should be reasonably accurate.

The well-conditioning of S implies the robustness of the direct approach with respect to spectral profile perturbations; cf. section 2.1. We present in Figure 4 the recoveries using imprecise spectral profiles for Example 6(i), where the spectral matrix is perturbed by additive Gaussian noise with a zero mean and standard deviation proportional to the entry magnitude. Even only with three frequencies, the recoveries remain stable up to 20% spectral perturbation, indicating the robustness of the approach, concurring with the findings in [48].

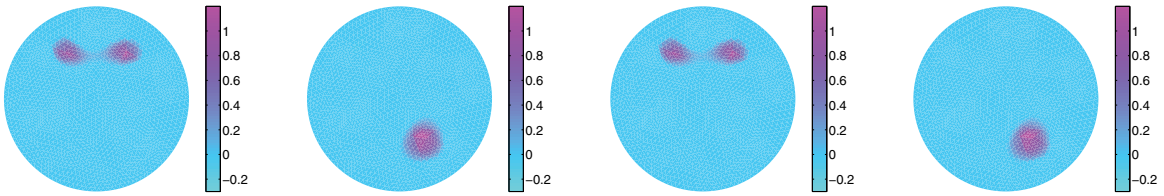

(a) recovered $\delta\sigma_1$ (b) recovered $\delta\sigma_2$ (c) recovered $\delta\sigma_1$ (d) recovered $\delta\sigma_2$

Figure 3. *Numerical results for Example* 6(i) *with different contact impedance constants,* 1% *data noise, and fully known* $s_k(\omega)$*s. The recoveries in* (a) *and* (b) *are obtained with* $z_j = 0.1$*,* $j = 1, \ldots, E$*, and those in* (c) *and* (d) *with* $z_j = 0.01$*,* $j = 1, \ldots, E$*, by the direct approach.*

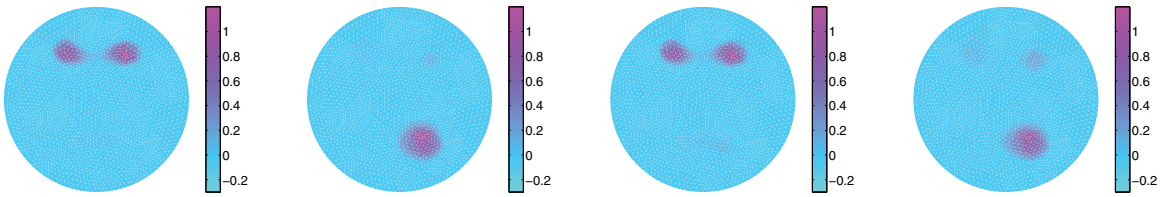

(a) recovered $\delta\sigma_1$ (b) recovered $\delta\sigma_2$ (c) recovered $\delta\sigma_1$ (d) recovered $\delta\sigma_2$

Figure 4. *Numerical results for Example* 6(i) *with* 1% *data noise and imprecisely known* $s_k(\omega)$*s. The recoveries in* (a) *and* (b) *are obtained with* S *perturbed by additive Gaussian noise with mean zero and standard deviation* 10% *of the entry magnitude, and those in* (c) *and* (d) *with* 20% *noise, both by the direct approach.*

Table 1

The relative errors for Example 6(i) *with various mesh size* h*, noise level* ϵ*, and regularization parameter* α*, where* $h_1 =$ 1.27e-1*,* $h_2 =$ 6.36e-2 *and* $h_3 =$ 3.18e-2*. The error is computed with respect to the reference solution, which is the recovery on the finest mesh.*

	$\alpha =$ 5-3			$\alpha =$ 1e-2			$\alpha =$ 5e-2		
ϵ	h_1	h_2	h_3	h_1	h_2	h_3	h_1	h_2	h_3
1e-3	5.57e-2	2.72e-2	1.22e-2	7.80e-2	3.85e-2	1.74e-2	2.42e-1	1.26e-1	5.87e-2
3e-3	5.61e-2	2.75e-2	1.23e-2	7.83e-2	3.87e-2	1.75e-2	2.42e-1	1.26e-1	5.88e-2
1e-2	5.77e-2	2.82e-2	1.27e-2	7.95e-2	3.94e-2	1.78e-2	2.42e-1	1.26e-1	5.89e-2

Throughout, we have assumed a fixed discretization for the linearized model. Due to the ill-posed nature of the problem, the recovery may vary with the discretization, due to discretization error, apart from the data noise (and inherent linearization error). With Example 6(i), we briefly illustrate the dependence of the relative error of the recovery on the mesh size h used for the inversion (cf. (4.5)), the noise level ϵ, and the regularization parameter α. The results are shown in Table 1 for various combinations of h, ϵ, and α. Just as expected, the relative error increases with h and ϵ, and the convergence is relatively independent of α within this range. A detailed convergence analysis with respect to the discretization parameter for EIT imaging with Tikhonov regularization can be found in [23, 50].

Since $s_2'(\omega)$ is small in Example 6(ii), we also illustrate difference imaging of section 2.2.1. The recovery of the first set of inclusions, in the absence of the knowledge of s_ks, is shown in

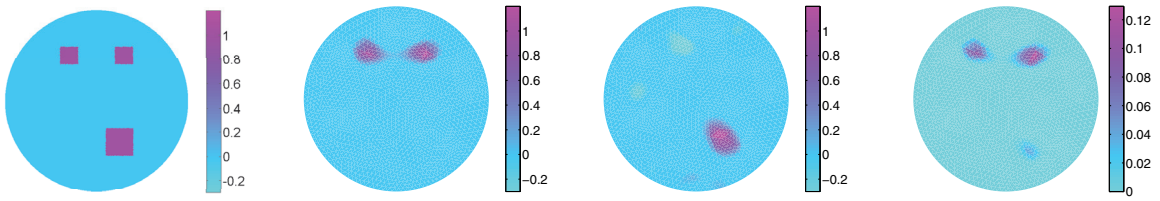

(a) true $\delta\sigma_k$s (b) recovered $\delta\sigma_1$ (c) recovered $\delta\sigma_2$ (d) recovered $\delta\sigma_1$

Figure 5. *Numerical results for Example* 6(ii) *with* 1% *data noise. The recoveries in* (b) *and* (c) *are obtained with known $s_k(\omega)$s using the direct approach and that in* (d) *without knowing $s_k(\omega)$s, using difference imaging.*

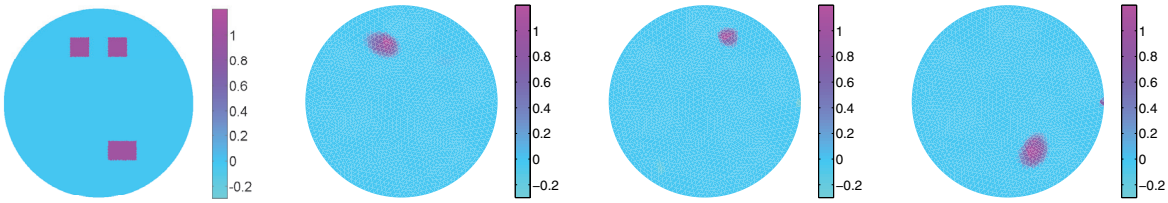

(a) true $\delta\sigma_k$s (b) recovered $\delta\sigma_1$ (c) recovered $\delta\sigma_2$ (d) recovered $\delta\sigma_3$

Figure 6. *Numerical results for Example* 7(i) *with* 1% *data noise, with fully known $s_k(\omega)$s. The recoveries are obtained by the direct approach.*

Figure 5(d). The recoveries are free from spurious oscillations. This shows the capability of difference imaging for spectral profiles with substantially different dependence on ω.

Example 7. Consider three rectangular inclusions on the top left, top right, and bottom of the disk with spectral profiles $s_1(\omega)$, $s_2(\omega)$, and $s_3(\omega)$, respectively; cf. Figure 6(a) for an illustration. In the experiments, we consider the following two cases:

(i) The spectral profiles are $s_1(\omega) = 0.2\omega + 0.2$, $s_2(\omega) = 0.1\omega^2$ and $s_3(\omega) = 0.2\omega + 0.1$.

(ii) The spectral profiles are $s_1(\omega) = 0.02\omega + 0.02$, $s_2(\omega) = 0.1\omega^2$ and $s_3(\omega) = 0.2\omega + 0.1$.

In either case, we take three frequencies, $\omega_1 = 0$, $\omega_2 = 0.5$, and $\omega_3 = 1$.

The numerical results for Examples 7(i) and 7(ii) are shown in Figures 6 and 7, respectively. If all three $s_k(\omega)$s are known, the use of three frequencies yields almost perfect separation of the inclusions using the direct method: the recovered inclusions are well clustered with correct supports and magnitudes. For Example 7(ii), $s_1(\omega)$ is much smaller, and thus the recovered $\delta\sigma_1$ is more susceptible to noise, whereas the other two are more stable.

The results in Figure 7 indicate that with known $s_2(\omega)$ and $s_3(\omega)$ and unknown $s_1(\omega)$, since $s_1'(\omega)$ is small, difference imaging can recover accurately both the magnitude and support of $\delta\sigma_2$ and $\delta\sigma_3$. These observations fully confirm the discussions in section 2.2.

Our next example illustrates the case of different conductivities for each inclusion.

Example 8. The setup of the example is identical with that of Example 7(i), except that the inclusions on the top left, top right, and bottom have conductivity perturbations of 1.5, 1, and 0.5, respectively.

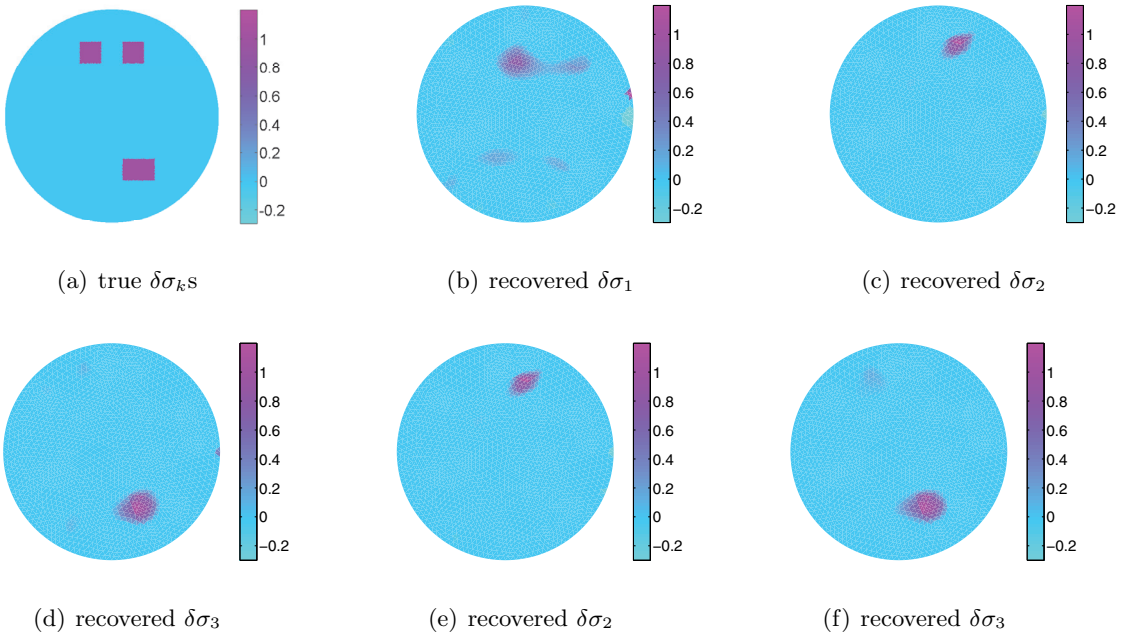

(a) true $\delta\sigma_k$s (b) recovered $\delta\sigma_1$ (c) recovered $\delta\sigma_2$

(d) recovered $\delta\sigma_3$ (e) recovered $\delta\sigma_2$ (f) recovered $\delta\sigma_3$

Figure 7. *Numerical results for Example 7*(ii) *with* 1% *data noise. Here* (b)–(d) *are the recoveries with fully known* $s_k(\omega)$ *and obtained by the direct approach, while for* (e) *and* (f) *only* $s_2(\omega)$ *and* $s_3(\omega)$ *are known, and the recoveries are obtained by difference imaging.*

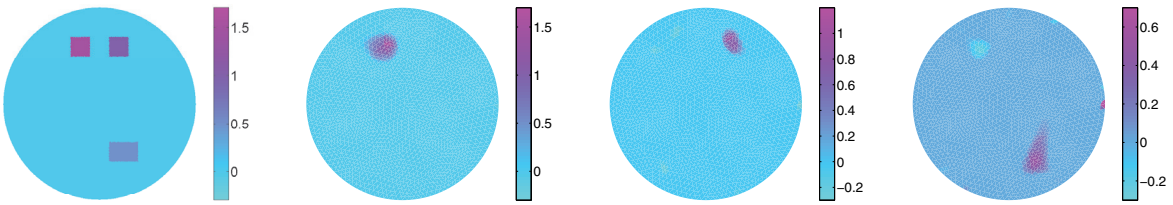

(a) true $\delta\sigma_k$s (b) recovered $\delta\sigma_1$ (c) recovered $\delta\sigma_2$ (d) recovered $\delta\sigma_3$

Figure 8. *Numerical results for Example 8 with* 1% *data noise, with fully known* $s_k(\omega)$*s. The recoveries are obtained by the direct approach.*

The numerical results are presented in Figure 8. With different conductivities for each inclusion, the reconstructions remain fairly reasonable: all three inclusions are well separated from each other, with their magnitudes accurately estimated, as in Example 7(i). However, the support of the inclusion on the bottom is slightly distorted; cf. Figure 8(d). This is attributed to the smaller magnitude of the inclusion, yielding a higher noise level of the corresponding linear inversion step, which deteriorates the reconstruction.

6.2. Imperfectly known boundary. Now we illustrate the approach in the case of an imperfectly known boundary. In the first example, the unknown true domain $\widetilde{\Omega}$ is an ellipse centered at the origin with semiaxes a and b, $\mathcal{E}_{a,b} = \{(x_1, x_2) : x_1^2/a^2 + x_2^2/b^2 < 1\}$, and the computational domain Ω is taken to be the unit circle.

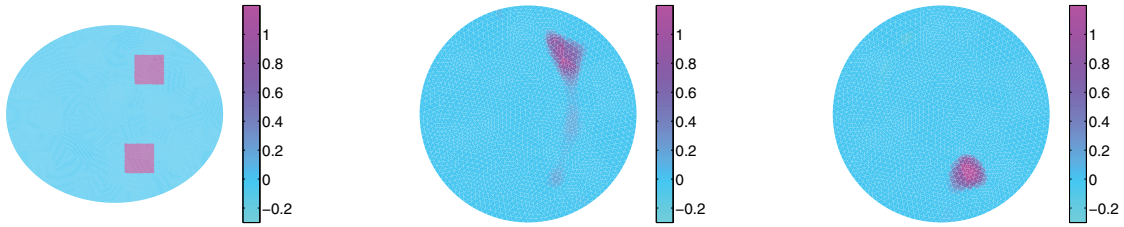

(a) true $\delta\sigma_k$s (b) recovered $\delta\sigma_1$ (c) recovered $\delta\sigma_2$

Figure 9. *Numerical results for Example* 9(i) *with* 0.1% *data noise, fully known* $s_k(\omega)$. *The recoveries are obtained using difference imaging.*

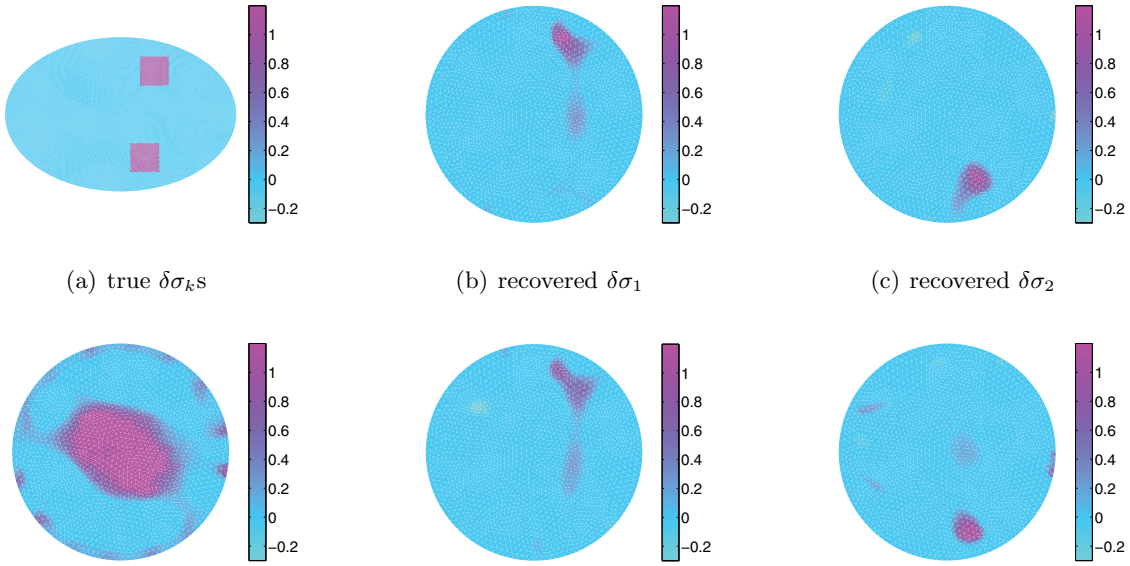

(a) true $\delta\sigma_k$s (b) recovered $\delta\sigma_1$ (c) recovered $\delta\sigma_2$

(d) recovered $\delta\sigma_0$ (e) recovered $\delta\sigma_1$ (f) recovered $\delta\sigma_2$

Figure 10. *Numerical results for Example* 9(ii) *with* 0.1% *data noise, fully known* $s_k(\omega)$*s. The recoveries in* (b)–(c) *are based on difference imaging, and those in* (d)–(f) *on the direct approach.*

Example 9. Consider two square inclusions on the top and the bottom of the ellipse, with $s_1(\omega) = 0.2\omega + 0.2$ and $s_2(\omega) = 0.1\omega^2$ (Figure 9). We consider the following two cases:

(i) The true domain $\widetilde{\Omega}$ is $\mathcal{E}_{a,b}$ with $a = 1.1$ and $b = 0.9$.

(ii) The true domain $\widetilde{\Omega}$ is $\mathcal{E}_{a,b}$ with $a = 1.2$ and $b = 0.8$.

In either case, we take three frequencies, $\omega_1 = 0$, $\omega_2 = 0.5$, and $\omega_3 = 1$.

The results are given in Figures 9 and 10 with 0.1% noise in the data, for Examples 9(i) and 9(ii), respectively. Although not presented, we note that the static imaging can only produce useless recoveries, due to the presence of significant modeling errors. Numerically one can verify that for both cases, the contribution from domain deformation is much larger than that of

the inclusions, which justifies the smaller noise level 0.1%. By exploiting the spectral incoherence, mfEIT can separate different contributions and hence recover each inclusion accurately.

From Figure 9, difference imaging can recover the inclusions accurately, and they are well separated, due to their incoherent $s_k(\omega)$s. However, the shape and location of the recovery tend to be slightly deformed. This concurs with the analysis in section 4: the unknown boundary induces deformed conductivity of the inclusions, in addition to the anisotropic component.

In Figure 10 we present the results related to Example 9(ii). The preceding observations on difference imaging still hold; cf. Figures 10(a) and 10(b). The direct approach works equally well: the recovered $\delta\sigma_1$ and $\delta\sigma_2$ are fairly accurate; and the results are comparable with those obtained by difference imaging. The recovered $\delta\sigma_0$ contains only the spurious conductivity induced by the domain deformation. Should there be any true inclusion $\delta\sigma_0$ corresponding to $s_0(\omega)$, it will be washed away by the error $\epsilon\Psi$; cf. (4.8). The preceding discussions fully confirm the analysis in section 4: mfEIT is capable of discriminating the perturbation due to domain deformation from the inclusions by either the direct approach or difference imaging.

Last we present one example where the electrodes are misplaced, but their lengths do not change, i.e., the factor z in the boundary integral can be set to the unit (see Example 5). This is a special case of the imperfectly known boundary case, where the forward map F maps the domain Ω onto itself. However, the forward map is not the identity or a rotation operator, and thus it will induce an anisotropic conductivity, especially in the regions near the boundary.

Example 10. The true domain $\widetilde{\Omega}$ is identical with the computational domain Ω, the unit circle, but every other electrode is shifted by an angle of $\pi/32$, while the length of each electrode remains unchanged; see Figure 1(b) for a schematic illustration. There are two rectangular inclusions, on the top and on the bottom of the ellipse, with spectral profiles $s_1(\omega) = 0.2\omega+0.2$ and $s_2(\omega) = 0.1\omega^2$, respectively. We take three frequencies $\omega_1 = 0$, $\omega_2 = 0.5$, and $\omega_3 = 1$.

The results for Example 10 are given in Figure 11. The analysis in section 4.2 indicates that the conductivity perturbation can be lumped to $\delta\sigma_0$. The results confirm the analysis: when using the direct approach, there are pronounced oscillations around the boundary in the recovered $\delta\sigma_0$. However, the recovered $\delta\sigma_1$ and $\delta\sigma_2$ are reasonable in both location and size. The difference imaging can also remove the contributions due to unknown electrode locations, since $s_k(\omega)$s are incoherent both before and after differentiation.

In summary, as expected from the analysis of sections 3 and 4.2, the mfEIT technique has significant potential in handling modeling errors. The inclusion $\delta\sigma_0$ corresponding to s_0 may not be recovered. However, by mfEIT, $\{\delta\sigma_k\}_{k=1}^K$ can be correctly recovered by either the direct approach or difference imaging, provided that s_ks or s_k's are sufficiently incoherent.

7. Concluding remarks.

In this paper we have presented novel reconstruction methods for multifrequency EIT. In particular, we have illustrated both analytically and numerically the significant potentials of mfEIT in handling the modeling error due to an imperfectly known boundary shape. We have also introduced a new and efficient group sparse reconstruction algorithm for the linearized EIT problem. The techniques may be extended to quantitative photoacoustic imaging from multispectral measurements [61].

This work represents only a first step toward the rigorous mathematical and numerical analysis of mfEIT. There are a few questions deserving further research. For instance, beyond

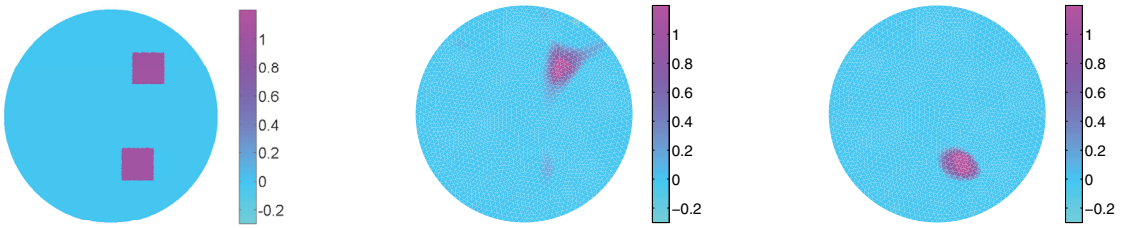

(a) true $\delta\sigma_i$s (b) recovered $\delta\sigma_1$ (c) recovered $\delta\sigma_2$

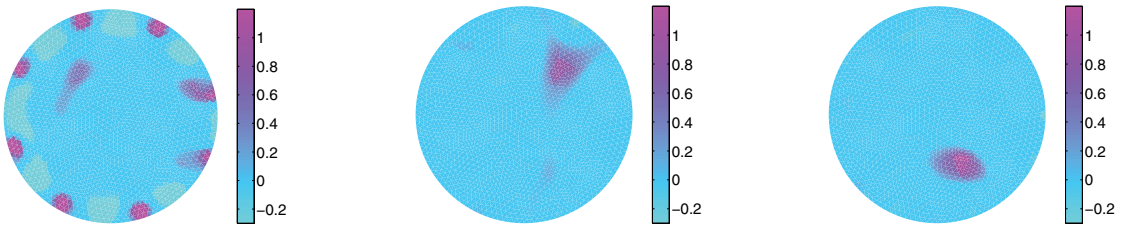

(d) recovered $\delta\sigma_0$ (e) recovered $\delta\sigma_1$ (f) recovered $\delta\sigma_2$

Figure 11. *Numerical results for Example 10 with* 0.1% *data noise, fully known* $s_k(\omega)$*s. The recoveries in* (b)–(c) *are based on difference imaging, and those in* (d)–(f) *on the direct approach.*

the linearized regime, the nonlinear approach may be more appropriate, but it comes with significant computational overhead, due to a large number of PDEs involved. It is imperative to develop fast image reconstruction algorithms and to provide theoretical justifications. Moreover, in this work we have mainly focused on the recovery of the abundances. It would be of great interest to derive sufficient conditions for the simultaneous recovery of partial spectral profiles, under suitable structural prior knowledge, e.g., the (disjoint) sparsity of abundances. It is expected that this issue may have different features in the nonlinear regime.

Acknowledgments. The authors are grateful to the anonymous referees and the associate editor Otmar Scherzer for their constructive comments, which have led to an improved presentation of the work.

REFERENCES

[1] A. Adler, R. Guardo, and Y. Berthiaume, *Impedance imaging of lung ventilation: Do we need to account for chest expansion?*, IEEE Trans. Biomed. Eng., 43 (1996), pp. 414–420.
[2] H. Ammari, *An Introduction to Mathematics of Emerging Biomedical Imaging*, Springer-Verlag, Berlin, 2008.
[3] H. Ammari, E. Bonnetier, Y. Capdeboscq, M. Tanter, and M. Fink, *Electrical impedance tomography by elastic deformation*, SIAM J. Appl. Math., 68 (2008), pp. 1557–1573.
[4] H. Ammari, S. Boulmier, and P. Millien, *A mathematical and numerical framework for magnetoacoustic tomography with magnetic induction*, J. Differential Equations, 259 (2015), pp. 5379–5405.
[5] H. Ammari, J. Garnier, L. Giovangigli, W. Jing, and J.-K. Seo, *Spectroscopic imaging of a dilute cell suspension*, J. Math. Pures Appl. (9), 105 (2016), pp. 603–661.

[6] H. Ammari, P. Grasland-Mongrain, P. Millien, L. Seppecher, and J.-K. Seo, *A mathematical and numerical framework for ultrasonically-induced Lorentz force electrical impedance tomography*, J. Math. Pures Appl. (9), 103 (2015), pp. 1390–1409.
[7] H. Ammari and H. Kang, *Reconstruction of Small Inhomogeneities from Boundary Measurements*, Springer-Verlag, Berlin, 2004.
[8] H. Ammari, O. Kwon, J.-K. Seo, and E.-J. Woo, *T-scan electrical impedance imaging system for anomaly detection*, SIAM J. Appl. Math., 65 (2004), pp. 252–266.
[9] H. Ammari, E. Lee, K. Kwon, J.-K. Seo, and E.-J. Woo, *Mathematical modeling of mechanical vibration-assisted conductivity imaging*, SIAM J. Appl. Math., 75 (2015), pp. 1031–1046.
[10] H. Ammari and J.-K. Seo, *An accurate formula for the reconstruction of conductivity inhomogeneities*, Adv. Appl. Math., 30 (2003), pp. 679–705.
[11] L. Borcea, *Electrical impedance tomography*, Inverse Problems, 18 (2002), pp. R99–R136.
[12] K.-S. Cheng, D. Isaacson, J. C. Newell, and D. G. Gisser, *Electrode models for electric current computed tomography*, IEEE Trans. Biomed. Eng., 36 (1989), pp. 918–924.
[13] Y. T. Chow, K. Ito, and J. Zou, *A direct sampling method for electrical impedance tomography*, Inverse Problems, 30 (2014), 095003.
[14] E. T. Chung, T. F. Chan, and X.-C. Tai, *Electrical impedance tomography using level set representation and total variational regularization*, J. Comput. Phys., 205 (2005), pp. 357–372.
[15] D. Colton and R. Kress, *Inverse Acoustic and Electromagnetic Scattering Theory*, Springer-Verlag, Berlin, 1992.
[16] I. Daubechies, M. Defrise, and C. De Mol, *An iterative thresholding algorithm for linear inverse problems with a sparsity constraint*, Comm. Pure Appl. Math., 57 (2004), pp. 1413–1457.
[17] P. J. Davis, *Interpolation and Approximation*, Blaisdell, New York, 1963.
[18] C. Gabriel, A. Peyman, and E. H. Grant, *Electrical conductivity of tissue at frequencies below* 1*MHz*, Phys. Med. Biol., 54 (2009), pp. 4863–4878.
[19] S. Gabriely, R. W. Lau, and C. Gabriel, *The dielectric properties of biological tissues:* II. *Measurements in the frequency range* 10 *Hz to* 20 *GHz*, Phys. Med. Biol., 41 (1996), pp. 2251–2269.
[20] B. Gebauer and O. Scherzer, *Impedance-acoustic tomography*, SIAM J. Appl. Math., 69 (2008), pp. 565–576.
[21] L. A. Geddes and L. E. Baker, *The specific resistance of biological material—A compendium of data for the biomedical engineeer and physiologist*, Med. Biol. Engng, (1967), pp. 271–293.
[22] M. Gehre and B. Jin, *Expectation propagation for nonlinear inverse problems—With an application to electrical impedance tomography*, J. Comput. Phys., 259 (2014), pp. 513–535.
[23] M. Gehre, B. Jin, and X. Lu, *An analysis of finite element approximation in electrical impedance tomography*, Inverse Problems, 30 (2014), 045013.
[24] E. Gersing, B. Hofmann, and M. Osypka, *Influence of changing peripheral geometry on electrical impedance tomography measurements*, Med. Biol. Eng. Comput., 34 (1996), pp. 359–361.
[25] J. F. Grcar, *Spectral condition numbers of orthogonal projections and full rank linear least squares residuals*, SIAM J. Matrix Anal. Appl., 31 (2010), pp. 2934–2949.
[26] H. Griffiths and A. Ahmed, *A dual-frequency applied potential tomography technique: Computer simulations*, Clin. Phys. Physiol. Meas., 8 (1987), pp. 103–107.
[27] B. Harrach and J.-K. Seo, *Detecting inclusions in electrical impedance tomography without reference measurements*, SIAM J. Appl. Math., 69 (2009), pp. 1662–1681.
[28] F. Hettlich, *Fréchet derivatives in inverse obstacle scattering*, Inverse Problems, 11 (1995), pp. 371–382.
[29] F. Hettlich, *Erratum: Fréchet derivatives in inverse scattering*, Inverse Problems, 14 (1998), pp. 209–210.
[30] R. Holm, *Electric Contacts: Theory and Applications*, Springer-Verlag, Berlin, 1967.
[31] J. Huang, X. Huang, and D. Metaxas, *Learning with dynamic group sparsity*, in Proceedings of the IEEE 12th International Conference on Computer Vision, 2009, pp. 64–71.
[32] J.-H. Hwang, K. S. Kirkpatrick, T. Mason, and E. Garboczi, *Experimental limitations in impedance spectroscopy: Part* IV. *Electrode contact effects*, Solid State Ionics, 98 (1997), pp. 93–104.
[33] K. Ito and B. Jin, *Inverse Problems: Tikhonov Theory and Algorithms*, World Scientific, Hackensack, NJ, 2014.

[34] B. Jin, T. Khan, and P. Maass, *A reconstruction algorithm for electrical impedance tomography based on sparsity regularization*, Internat. J. Numer. Methods Engrg., 89 (2012), pp. 337–353.
[35] B. Jin, D. A. Lorenz, and S. Schiffler, *Elastic-net regularization: Error estimates and active set methods*, Inverse Problems, 25 (2009), 115022.
[36] B. Jin and P. Maass, *An analysis of electrical impedance tomography with applications to Tikhonov regularization*, ESAIM Control Optim. Calc. Var., 18 (2012), pp. 1027–1048.
[37] J. P. Kaipio, V. Kolehmainen, E. Somersalo, and M. Vauhkonen, *Statistical inversion and Monte Carlo sampling methods in electrical impedance tomography*, Inverse Problems, 16 (2000), pp. 1487–1522.
[38] N. Keshava and J. F. Mustard, *Spectral unmixing*, IEEE Signal Proc. Mag., 19 (2002), pp. 44–57.
[39] S. Kim and A. Tamasan, *Reconstructing small perturbations in electrical admittivity at low frequencies*, Inverse Problems, 30 (2014), 035006.
[40] V. Kolehmainen, M. Lassas, and P. Ola, *The inverse conductivity problem with an imperfectly known boundary*, SIAM J. Appl. Math., 66 (2005), pp. 365–383.
[41] V. Kolehmainen, M. Lassas, and P. Ola, *Electrical impedance tomography problem with inaccurately known boundary and contact impedances*, IEEE Trans. Med. Imag., 27 (2008), pp. 1404–1414.
[42] O. Kwon, J.-K. Seo, and J.-R. Yoon, *A real-time algorithm for the location search of discontinuous conductivities with one measurement*, Comm. Pure Appl. Math., 55 (2002), pp. 1–29.
[43] S. Laufer, A. Ivorra, V. E. Reuter, B. Rubinsky, and S. B. Solomon, *Electrical impedance characterization of normal and cancerous human hepatic tissue*, Physiol. Meas., 31 (2010), pp. 995–1009.
[44] A. Lechleiter, *The MUSIC algorithm for impedance tomography of small inclusions from discrete data*, Inverse Problems, 31 (2015), 095004.
[45] A. Lechleiter and A. Rieder, *Newton regularizations for impedance tomography: A numerical study*, Inverse Problems, 22 (2006), pp. 1967–1987.
[46] W. Lionheart, *EIT reconstruction algorithms: Pitfalls, challenges and recent developments*, Physiol. Meas., 25 (2004), pp. 125–142.
[47] E. Malone, G. Sato dos Santos, D. Holder, and S. Arridge, *Multifrequency electrical impedance tomography using spectral constraints*, IEEE Trans. Med. Imag., 33 (2014), pp. 340–350.
[48] E. Malone, G. Sato dos Santos, D. Holder, and S. Arridge, *A reconstruction-classification method for multifrequency electrical impedance tomography*, IEEE Trans. Med. Imag., 34 (2015), pp. 1486–1497.
[49] C. Pöschl, E. Resmerita, and O. Scherzer, *Discretization of variational regularization in Banach spaces*, Inverse Problems, 26 (2010), 105017.
[50] L. Rondi, *Discrete approximation and regularisation for the inverse conductivity problem*, Rend. Istit. Mat. Univ. Trieste, 2016, in press; also available online from http://www.dmi.units.it/~rondi/psfiles/discrete.pdf.
[51] L. Rondi and F. Santosa, *Enhanced electrical impedance tomography via the Mumford-Shah functional*, ESAIM Control Optim. Calc. Var., 6 (2001), pp. 517–538.
[52] O. Scherzer, M. Grasmair, H. Grossauer, M. Haltmeier, and F. Lenzen, *Variational Methods in Imaging*, Springer-Verlag, Berlin, 2009.
[53] J. Schlappa, E. Annese, and H. Griffiths, *Systematic errors in multi-frequency EIT*, Physiol. Meas., 21 (2000), pp. 111–118.
[54] T. Schuster, B. Kaltenbacher, B. Hofmann, and K. S. Kazimierski, *Regularization Methods in Banach Spaces*, Walter de Gruyter, Berlin, 2012.
[55] J. K. Seo, J. Lee, S. W. Kim, H. Zribi, and E. J. Woo, *Frequency-difference electrical impedance tomography (fdEIT): Algorithm development and feasibility study*, Physio. Meas., 29 (2008), pp. 929–944.
[56] J.-K. Seo and E.-J. Woo, *Magnetic resonance electrical impedance tomography (MREIT)*, SIAM Rev., 53 (2011), pp. 40–68.
[57] S. Siltanen, J. Mueller, and D. Isaacson, *An implementation of the reconstruction algorithm of A. Nachman for the 2D inverse conductivity problem*, Inverse Problems, 16 (2000), pp. 681–699.
[58] E. Somersalo, M. Cheney, and D. Isaacson, *Existence and uniqueness for electrode models for electric current computed tomography*, SIAM J. Appl. Math., 52 (1992), pp. 1023–1040.

[59] A. J. Surowiec, S. S. Stuchly, J. R. Barr, and A. Swarup, *Dielectric properties of breast carcinoma and the surrounding tissues*, IEEE Trans. Biomed. Eng., 35 (1988), pp. 257–263.
[60] J. Sylvester, *An anisotropic inverse boundary value problem*, Comm. Pure Appl. Math., 43 (1990), pp. 201–232.
[61] A. Taruttis and V. Ntziachristos, *Advances in real-time multispectral optoacoustic imaging and its applications*, Nature Photonics, 9 (2015), pp. 219–227.
[62] K. Vervier, P. Mahé, D'Aspremont, J.-B. Veyrieras, and J.-P. Vert, *On learning matrices with orthogonal columns or disjoint supports*, Lect. Notes in Comput. Sci. 8726, Springer-Verlag, Berlin, 2014, pp. 274–289.
[63] R. J. Yerworth, R. H. Bayford, B. Brown, P. Milnes, M. Conway, and D. S. Holder, *Electrical impedance tomography spectroscopy (EITS) for human head imaging*, Physiol. Meas., 24 (2003), pp. 477–489.